CORE
Metadata, citation and similar papers at core.ac.uk
Provided by Illinois Digital Environment for Access to Learning and Scholarship Repository

© 2010 Zuhaib Bashir Sheikh

NUMERICAL MODELING OF MULTI-CONDUCTOR INTERCONNECTS FOR HIGH SPEED INTEGRATED CIRCUITS

BY

ZUHAIB BASHIR SHEIKH

THESIS

Submitted in partial fulfillment of the requirements
for the degree of Master of Science in Electrical and Computer Engineering
in the Graduate College of the
University of Illinois at Urbana-Champaign, 2010

Urbana, Illinois

Adviser:

Professor Andreas C. Cangellaris

ABSTRACT

Presented here is an alternative methodology to the development of transmission line models for multi-conductor interconnects in high speed integrated circuits. The methodology starts with the assumption that per unit length (p.u.l.) transmission line parameters — i.e. p.u.l. resistance $\mathcal{R}$, inductance $\mathcal{L}$, capacitance $\mathcal{C}$, and conductance $\mathcal{G}$ — have been extracted using a two-dimensional RLCG extractor. The methodology relies upon a rational fitting algorithm called VECTFIT to express the parameters as a rational function expression, a form suitable for equivalent circuit generation using a commercial circuit simulator like HSPICE. The methodology has been numerically verified and implemented in the form of some select interconnecting scenarios for typical on-chip applications. The new methodology has also been compared with the previous methodology for robustness, accuracy and computational efficacy.

To my Parents, My First Teachers

ACKNOWLEDGMENTS

First and foremost I would like to praise and thank God Almighty who has been showering his innumerable bounties upon me since the day I came as a helpless individual into this world. It is His utmost favor upon me that He provided me with the best adviser I could aspire for in the person of Prof. Andreas Cangellaris. Prof. Cangellaris' patient advice and insightful guidance have made this work possible and I consider myself deeply indebted to him for the rest of my life. His insightful discourses and discussions helped me look beyond the obvious mathematical concepts and dig deep into the underlying physical phenomena all the way to their engineering applications. I consider it a privilege to have been a part of his group.

Additionally, I would like to acknowledge all the faculty and staff of the ECE department for their support, guidance, and wisdom. I am also extremely grateful to the Center for Computational Electromagnetics and Electromagnetics Laboratory faculty, especially Prof. José Schutte Ainé, Prof. Jianming Jin and Prof. Jennifer Bernhard for their influence on my academic life during my graduate studies. I am especially grateful to Dr. Irfan Ahmad, Dr. Nahil Sobh and Prof. Umberto Ravaioli from the Micro and Nanotechnology Lab for their support.

My friends and colleagues from the campus community have been an invaluable part of my life at the University of Illinois. I am particularly grateful to Mohamed Mohamed, Azeem Sarwar and Naeem Sheikh for providing me with the much needed motivational inputs and useful tips. I am also thankful to my colleagues in Prof. Cangellaris' group — especially Prasad Sumant, Hong Wu, Ata Zadehgol, Jason Chung,

Joon Chung, Se Jung Moon, Anne Woo, and Anand and Aravind Ramachandran — for their valuable help and encouragement throughout.

Finally, and most importantly, I would like to express my deepest gratitude to my parents. Their constant encouragement, unfailing support and boundless love have always been a source of strength and inspiration throughout my life.

TABLE OF CONTENTS

CHAPTER 1

INTRODUCTION

The evolution of digital systems over the years has seen a congruent growth in the importance given to the physics and modeling of the involved active devices. However, a continuing trend of increasing clock rates in integrated and packaged electronic systems has shifted the paradigm of design and efficiency from device-centricity to wire-centricity. During the early years of digital computing when the clock frequency of digital systems was less than 100 MHz, the layout design methods for signaling wires and packages remained very impervious to the electrical properties of the interconnects. As such, the design decisions regarding signal wires were mostly concerned with the actual mapping of interconnects on a dual-layer board and ensuring that the packages stay sturdy through the assembly process [1]. However, for clock frequencies higher than 100 MHz or rise times shorter than 1 ns, also referred to as the high-frequency or high-speed regime, the electrical properties of the interconnects gained prominence owing to their loss of transparency to the propagating signals and hence the electromagnetic effects could no longer be ignored or roughly approximated. With the clock rates ticking well into the gigahertz range, the need to understand the problems that arise in products and systems dealing with such high-speed interconnects has led to the evolution of the engineering discipline known as *signal integrity*. The origin of signal-integrity issues can be traced back to the physical nature of the interconnects and packages, which could be simplified to connection lines or wires at low frequencies but have to be dealt with as transmission lines at high frequencies. In addition, antenna effects come into play leading

to cross-talk and electromagnetic interference (EMI). It is imperative for a signal-integrity engineer to fully comprehend the symptoms and identify the origins of these effects. Having done so, the next step is to accurately model them and incorporate them into the chip simulation to ensure accuracy of simulation and validate the design process. Further modifications can be made to the model to meet the signal integrity specifications without compromising the logic functionality of the involved digital circuitry [2].

Assessing performance of signal transmission in signal-integrity analysis of complex interconnects and packaging structures in integrated circuit design requires an accurate modeling of the multi-GHz wave-propagation. The developed models must account for delays due to electromagnetic retardation, wave-reflection due to impedance discontinuities and the incorporation of skin effect to accurately depict the frequency-dependent conductor losses and dispersion effects. The fact that the electromagnetic fields that constitute the signal transmission are distributed mostly along the interconnect axis enables us to model them using transmission line theory. This is true for interconnect sections which are long compared to the effective cross-sectional dimensions. However, for cross-sections smaller than the minimum wavelength, transverse electromagnetic mode (TEM) or quasi-TEM wave propagation is ensured [3]. It has been shown in [4-6] that generalized telegrapher's equation based quasi-TEM modeling of multi-conductor buses, both at the chip and board levels, can be used without any loss of accuracy for the prediction of electromagnetic wave propagation. Hence, these equations can be used for broadband signal transmission modeling and simulation if the per unit length resistance $\mathcal{R}$, inductance $\mathcal{L}$, capacitance $\mathcal{C}$, and conductance $\mathcal{G}$ have already been extracted. This is based upon the presumption that the effects due to the geometry of the interconnect, its

material properties and the surrounding environment have been captured by these per unit length parameters [7].

A significant amount of work has already been done in the development of multi-conductor transmission line (MTL) models in high speed interconnect and package analysis. In [8], the development of a new broadband transmission line model for accurate simulation of dispersive interconnects has been discussed in detail. The methodology discussed in the paper has been implemented in the form of a two-dimensional RLCG extractor called UIUC2D which also synthesizes a SPICE compatible passive lumped equivalent circuit for the input-output characteristics of the interconnect, such as per unit length impedance and admittance matrices [9]. The work presented in this thesis presents a modified approach towards the SPICE netlist generation [10]. As discussed in Chapter 2, both model development approaches start with the rational function approximation of the input-output characteristics of the interconnects to yield a pole/residue representation of the per unit length impedance and admittance matrices. This representation facilitates the implementation of a variety of numerical schemes for transmission line analysis in the frequency and time domains [8]. Chapter 3 demonstrates the implementation of the proposed numerical scheme, called *π-network topology* in this thesis, while highlighting the differences from the previously implemented one which has been named the *UIUC2D* approach. The simulation results obtained from the application of both approaches have been compared in light of computational efficiency and robustness in Chapter 4. Chapter 5 discusses future work that can be done in reducing the order of the developed discrete models for dispersive multi-conductor interconnects by utilizing their compatibility with passive model order reduction algorithms.

CHAPTER 2

BACKGROUND: MACRO-MODEL GENERATION

2.1 Introduction

Black-box modeling enables the construction of macro-models which give an accurate representation of the terminal behavior of a network without the need to delve into the physical basis of such a representation. This provides the ability to model elaborate physical devices with relatively simpler mathematical models with little or no loss in accuracy, thereby reducing the computational time needed to accurately depict their behavior in the physical domain [11]. The work presented in this chapter discusses the application of VECTFIT to express the elements of $\mathbf{R_{pul}}(\boldsymbol{\omega})$, $\mathbf{L_{pul}}(\boldsymbol{\omega})$, $\mathbf{C_{pul}}(\boldsymbol{\omega})$ and $\mathbf{G_{pul}}(\boldsymbol{\omega})$ (or simply $\mathcal{R}$, $\mathcal{L}$, $\mathcal{C}$ and $\mathcal{G}$), generated by UIUC2D as a closed form rational expression. VECTFIT is a robust algorithm which allows a very broad range of network responses to be fitted accurately by a rational function [12]. The pole/residue form of the rational function facilitates the development of passive lumped frequency-dependent equivalent circuits that model the geometry and material properties of the MTL and its surrounding environment.

2.2 The Telegrapher's Equations for an MTL

The generalized telegrapher's equations give a very accurate representation of either transverse electromagnetic wave (TEM) or quasi-TEM wave propagation. For the case of a multi-conductor interconnect modeled as an MTL, the telegrapher's equations can be written in the frequency domain as:

$$-\frac{\partial}{\partial z}\,\mathbf{V}(z,\omega) = \left[\mathbf{R_{pul}}(\omega) + j\omega\,\mathbf{L_{pul}}(\omega)\right]\mathbf{I}(z,\omega) \tag{2.1}$$

$$-\frac{\partial}{\partial z}\,\mathbf{I}(z,\omega) = \left[\mathbf{G_{pul}}(\omega) + j\omega\,\mathbf{C_{pul}}(\omega)\right]\mathbf{V}(z,\omega) \tag{2.2}$$

where $\mathbf{R_{pul}}(\omega)$, $\mathbf{L_{pul}}(\omega)$, $\mathbf{C_{pul}}(\omega)$ and $\mathbf{G_{pul}}(\omega)$ are the appropriate per unit length (p.u.l.) frequency-dependent square matrices of size N_c for the interconnect with N_c conductors and a common ground plane. These parameters can be generated from any RLGC parasitic extractor, which in our case is UIUC2D. After extracting the $\boldsymbol{\mathcal{R}}$, $\boldsymbol{\mathcal{L}}$, $\boldsymbol{\mathcal{C}}$ and $\boldsymbol{\mathcal{G}}$ matrices, the discrete frequency-dependent p.u.l. series impedance and the p.u.l. shunt admittance of the MTL can be written as $\mathbf{Z_{pul}}(\omega) = \mathbf{R_{pul}}(\omega) + j\omega\,\mathbf{L_{pul}}(\omega)$ and $\mathbf{Y_{pul}}(\omega) = \mathbf{G_{pul}}(\omega) + j\omega\,\mathbf{C_{pul}}(\omega)$, respectively. The $\mathbf{Z_{pul}}(\omega)$ and $\mathbf{Y_{pul}}(\omega)$ matrices relate the vector of voltages (or $\mathbf{V}(z,\omega)$) for the N_c conductors with respect to the common ground with the vector of N_c conductor currents (or $\mathbf{I}(z,\omega)$) using the simplified form of the MTL Equations (2.1) and (2.2) in the frequency domain:

$$-\frac{\partial}{\partial \mathrm{z}}\,\mathbf{V}(z,\omega) = \mathbf{Z_{pul}}(\omega)\,\mathbf{I}(z,\omega) \tag{2.3}$$

$$-\frac{\partial}{\partial \mathrm{z}}\,\mathbf{I}(z,\omega) = \mathbf{Y_{pul}}(\omega)\,\mathbf{V}(z,\omega) \tag{2.4}$$

The MTL under consideration is divided into several sections of equal length $\Delta z = h$, such that h is a suitable fraction of the wavelength corresponding to the highest frequency in the bandwidth of interest. In order to transform the differential Equations (2.3) and (2.4) to difference Equations (2.7) and (2.8), each of the smaller sections of the MTL is described by the matrices $\mathbf{Z_h}$ and $\mathbf{Y_h}$ in terms of $\mathbf{Z_{pul}}$ and $\mathbf{Y_{pul}}$ using Equations (2.5) and (2.6), respectively.

$$\mathbf{Z_h}(\omega) \triangleq h\,\mathbf{Z_{pul}}(\omega) \tag{2.5}$$

$$\mathbf{Y_h}(\omega) \triangleq h\,\mathbf{Y_{pul}}(\omega) \tag{2.6}$$

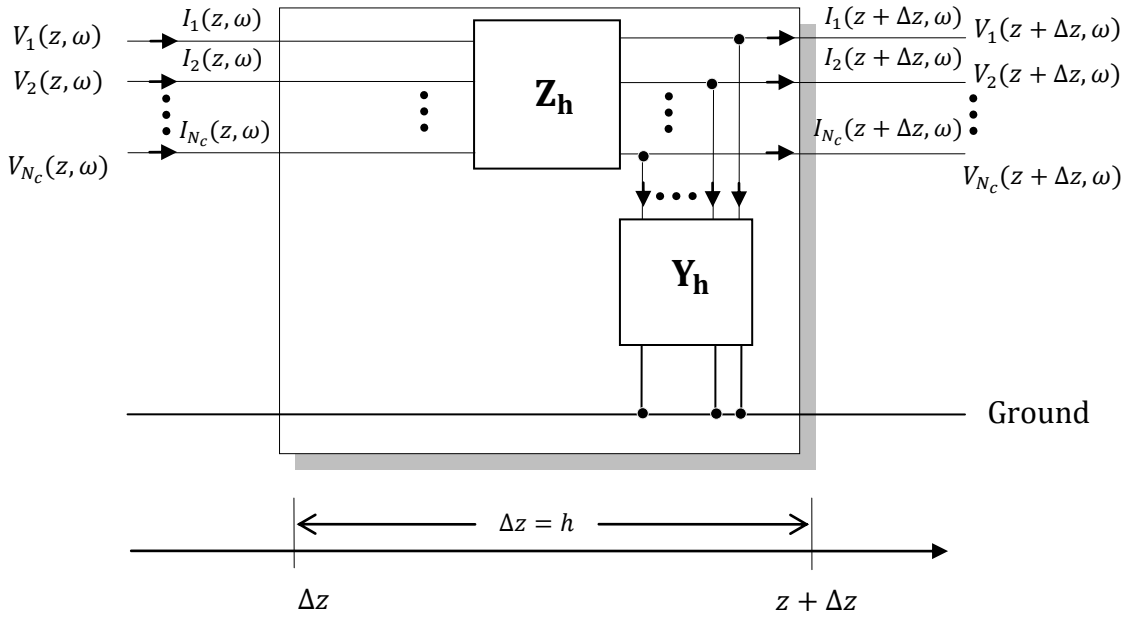

Figure 2.1: L-shaped implementation of the MTL telegrapher's equation

The resulting difference equations satisfy Kirchhoff's voltage and current laws around the loop in Figure 2.1.

$$\mathbf{V}(z,\omega) - \mathbf{V}(z+\Delta z,\omega) = \mathbf{Z_h}(\omega)\,\mathbf{I}(z,\omega) \tag{2.7}$$

$$\mathbf{I}(z,\omega) - \mathbf{I}(z+\Delta z,\omega) = \mathbf{Y_h}(\omega)\,\mathbf{V}(z+\Delta z,\omega) \tag{2.8}$$

The matrices $\mathbf{Z}_\mathrm{h}$ and $\mathbf{Y_h}$ can be represented as closed form rational function expressions using matrix fitting computer code [13] to yield the approximate matrices $\mathbf{Z_{h\_fit}}$ and $\mathbf{Y_{h\_fit}}$. At the core of the matrix fitting algorithm is the VECTFIT algorithm, which allows us to fit all the elements of a vector simultaneously using a common set of poles [12]. This relationship between matrices $\mathbf{Z_h}$, $\mathbf{Y_h}$ and $\mathbf{Z_{h\_fit}}$, $\mathbf{Y_{h\_fit}}$ can be written in the Laplacian domain as Equations (2.9) and (2.10), respectively:

$$\mathbf{Z_h}(s) \cong \mathbf{Z_{h\_fit}}(s) = \mathbf{R_0} + s\mathbf{L_0} + \sum_{k=1}^{K_1} \frac{\mathbf{R_k}}{s - P_k} \tag{2.9}$$

$$\mathbf{Y_h}(s) \cong \mathbf{Y_{h\_fit}}(s) = \mathbf{G_0} + s\mathbf{C_0} + \sum_{k=1}^{K_2} \frac{\mathbf{G_k}}{s - Q_k} \tag{2.10}$$

where $s = j\omega$.

It must be noted that the network is realizable if all P_k and Q_k are negative, $\mathbf{R_0}$ and $\mathbf{G_0}$ are positive definite, and all of the elements of $\mathbf{L_0}$ are positive. Equations (2.9) and (2.10) in expanded form can be represented as:

$$Z_h^{(ij)}(s) \cong Z_{h\_fit}^{(ij)}(s) = {R_0}^{(ij)} + s{L_0}^{(ij)} + \sum_{k=1}^{K_1} \frac{R_k^{(ij)}}{s - P_k}, \quad i,j = 1,2,\ldots.,N \tag{2.11}$$

$$Y_h^{(ij)}(s) \cong Y_{h\_fit}^{(ij)}(s) = {G_0}^{(ij)} + s{C_0}^{(ij)} + \sum_{k=1}^{K_2} \frac{G_k^{(ij)}}{s - Q_k}, \quad i,j = 1,2,\ldots.,N \tag{2.12}$$

In performing this fit, one common set of poles is used to fit all the elements of the $\mathbf{Z_h}$ matrix and another set for the $\mathbf{Y_h}$ matrix. Equations (2.9) and (2.10) are the closed form rational expressions of the approximate impedance and admittance matrices $\mathbf{Z_{h\_fit}}$ and $\mathbf{Y_{h\_fit}}$, respectively, and constitute the macro-model generated by the fitting algorithm. As such, they incorporate the magneto-quasi-static and electro-quasi-static effects of the physical interaction between the conductors in the transverse directions. It is, therefore, natural to expect one set of poles to describe all the elements in the matrix which has been rigorously defined as a well-known boundary-value problem [8,9].

It should be noted that only real poles are required to fit the matrices $\mathbf{Z_h}$ and $\mathbf{Y_h}$, respectively, since the length of the transmission line segment represented by matrices $\mathbf{Z_h}$ and $\mathbf{Y_h}$ is a small fraction of the minimum wavelength. Thus, it is sufficient to include

only real poles P_k and Q_k in the rational expressions in Equations (2.9) and (2.10), respectively.

2.3 Passivity and Stability

Since the media involved in the calculation of $\mathbf{Z}_{\text{pul}}$ and $\mathbf{Y}_{\text{pul}}$ are passive by nature, the matrices are necessarily passive. This requires that the poles in (2.9) and (2.10) should lie in the left half of the complex *s* plane. VECTFIT provides a feature in which the stability of the synthesized model can be ensured by flipping the unstable poles to the left half plane during the fitting process. VECTFIT also checks for passivity enforcement during synthesis of the generated macro-models [14].

CHAPTER 3

METHODOLOGY: EQUIVALENT CIRCUIT GENERATION

3.1 Introduction

This chapter discusses the second step in the incorporation of the frequency-dependent attributes of the passive interconnect network into nonlinear, network analysis-oriented circuit simulators like SPICE. After the per unit length (p.u.l.) matrices $\mathbf{R_{pul}}(\omega)$, $\mathbf{L_{pul}}(\omega)$, $\mathbf{C_{pul}}(\omega)$ and $\mathbf{G_{pul}}(\omega)$ have been expressed as pole/residue forms in Equations (2.9) and (2.10), the next step is the development of the transmission line models for transient simulation. Equations (2.9) and (2.10) can be combined in various ways to formulate many different implementation schemes of the MTL macro-model which are compatible with a wide class of SPICE-based transient circuit simulators. This chapter first describes the scheme previously implemented in UIUC2D software packages in Section 3.2 and then discusses the development of the proposed new implementation in Section 3.3.

3.2 The UIUC2D Mutual Inductances Implementation Scheme

For the case of the frequency-dependent p.u.l impedance matrix, the development of such a form is based on the modal network theory of the skin effect in lossy conductors [15]. According to this theory, the frequency dependence of the current distribution inside a lossy conductor can be described in terms of an equivalent network of resistors and inductors whose impedance is consistent with the form presented in

Equation (2.9).

Rewriting Equation (2.9) as (3.1):

$$\mathbf{Z_{pul}}(s) \cong \mathbf{R_0} + s\mathbf{L_0} + \sum_{k=1}^{K_1} \frac{\mathbf{R_k}}{s - P_k} \tag{3.1}$$

It must be noted that the network is realizable if all P_k are negative, $\mathbf{R_0}$ is positive definite and all of the elements of $\mathbf{L_0}$ are positive. Equation (3.1) can be rearranged as:

$$\mathbf{Z_{pul}}(s) \cong \bar{\mathbf{R}}_\mathbf{0} + s\mathbf{L_0} + \sum_{k=1}^{K_1} \frac{s}{s - P_k} \; \overline{\mathbf{R_k}}$$

$$\bar{\mathbf{R}}_\mathbf{0} = \mathbf{R_0} - \sum_{k=1}^{K_1} \frac{1}{P_k} \mathbf{R_k} \qquad \overline{\mathbf{R_k}} = \frac{\mathbf{1}}{P_k} \; \mathbf{R_k} \qquad \overline{\mathbf{L_k}} = -\frac{\mathbf{1}}{P_k} \; \overline{\mathbf{R_k}} \tag{3.2}$$

The development of this scheme has been described in [16]. With s approaching zero in (3.1), all terms of $\mathbf{Z_h}(s = 0)$ tend to zero except $\bar{\mathbf{R}}_\mathbf{0}$. Therefore, $\mathbf{Z_h}(s = 0) = \bar{\mathbf{R}}_\mathbf{0}$ is the diagonal matrix that represents the p.u.l. DC resistance matrix. With s approaching infinity, the terms in the summation over k approach $\bar{\mathbf{R}}_\mathbf{k}$. As a result, $\mathbf{L_0}$ is then the p.u.l. external inductance, since the summation over k is purely resistive at high frequencies. Each element of $\mathbf{Z_h}$ is then realized by the circuit shown in Figure 3.1.

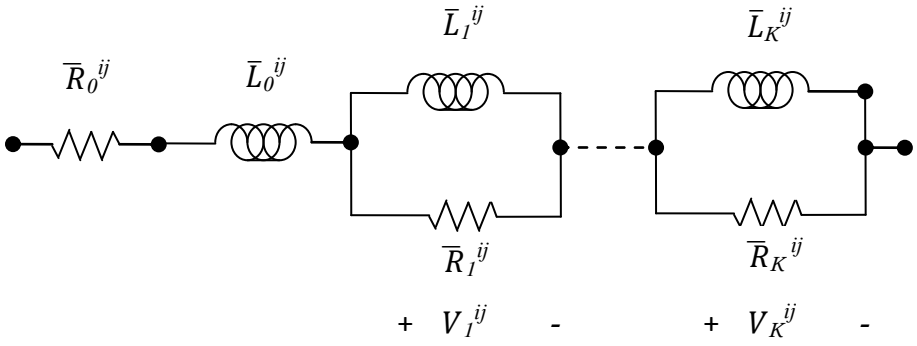

Figure 3.1: Representation of each element of $\mathbf{Z_h}$ using UIUC2D approach

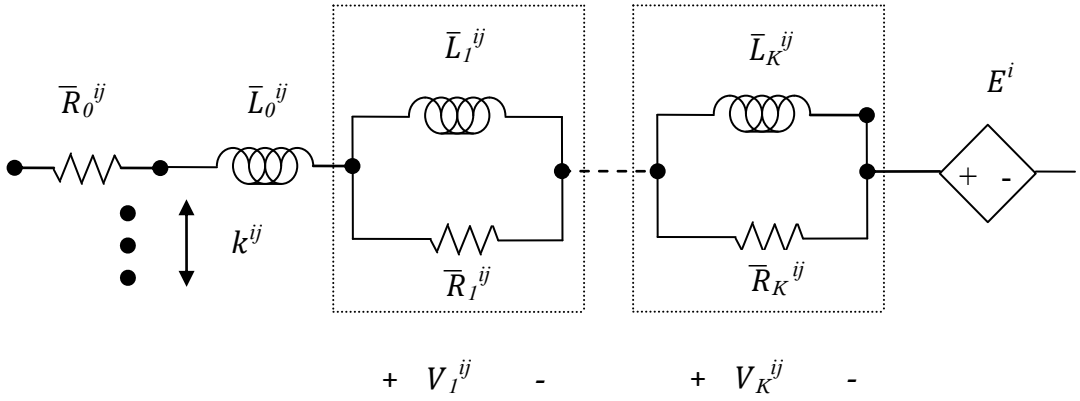

Figure 3.2: Representation of equivalent circuit for each conductor

The p.u.l. equivalent circuit for each of the N_c conductors is shown in Figure 3.2. The circuit is constructed by starting with the circuit in Figure 3.1 for the self-impedance. The addition of the off-diagonal elements of $\mathbf{L_0}$ is represented as mutual inductance coefficients

$$k^{ij} = \frac{L_0^{ij}}{\sqrt{L_0^{ii}\, L_0^{ij}}} \quad i \neq j \tag{3.3}$$

The addition of the off-diagonal elements of $\bar{\mathbf{R}}_\mathbf{k}$ is represented as a voltage-dependent voltage-source E_i. Since the same set of poles are used in the characterization of every $Z_{h_{ij}}$, the off-diagonal elements of $\bar{\mathbf{R}}_\mathbf{k}$ are proportional to each of the $\left(\bar{R}_k^{ii}, \bar{L}_k^{ii}\right)$ pairs. As a result, the voltage drop V_k^{ij} is simply a scaling in magnitude of the voltage drop V_k^{ij}. Therefore, the voltage drop due to $\bar{R}_k^{ij}$ can be realized by

$$V_k^{ij} = \frac{\bar{R}_k^{ij}}{\bar{R}_k^{jj}} V_k^{jj} \tag{3.4}$$

This now defines the coupling between off-diagonal residues by reusing the self-term

circuit-element quantities from Figure 3.1. The voltage source E_i is then the sum of voltage drops due to all coupled line residues, or

$$E_i = \sum_{j=1}^{K} \sum_{k=1}^{K1} V_k^{ij} \quad i \neq j \tag{3.5}$$

The complex impedance of each conductor in a p.u.l. section of the MTL system is generically modeled by the circuit shown in Figure 3.2. It is important to emphasize that this SPICE-compatible p.u.l. equivalent circuit captures the frequency-dependent behaviors of $\mathbf{R_{pul}}(\omega)$ and $\mathbf{L_{pul}}(\omega)$, including all off-diagonal coupling terms, for an MTL system.

For the sake of completeness, the dual closed form for the frequency-dependent admittance matrix $\mathbf{Y_{pul}}(s) = \mathbf{G_{pul}}(s) + s\,\mathbf{C_{pul}}(s)$ is given by

$$\mathbf{Y_{pul}}(s) \cong \mathbf{G_0} + s\,\mathbf{C_0} + \sum_{k=1}^{K_2} \frac{\mathbf{G_k}}{s - Q_k} \tag{3.6}$$

In the actual implementation of the UIUC2D software, however, the $\mathbf{G_{pul}}$ and $\mathbf{C_{pul}}$ are assumed to be independent of frequency. This simplifies the network realization considerably for the admittance matrix, and exempts the $\mathbf{Y_{pul}}$ matrix from being subjected to the rigorous fitting algorithm and the consequent equivalent circuit generation, thereby limiting the circuit size for circuit simulators. However, this does affect the accuracy of the transmission line model for the case where the dielectric media electrical properties exhibit frequency dependence and/or departure of the fields from the quasi-TEM behavior is significant. Such cases are not captured by the model.

3.3 The π–Network Topology Scheme

The motivation for this approach comes from combining Equations (2.9) and (2.10) in a form such that the symmetry of the transmission line model generated as a result is preserved. It should be noted that in our implementation, the inclusion of the series inductance matrix $\mathbf{L_0}$ and the series capacitance matrix $\mathbf{C_0}$ resulted in rank-deficiency in some of the intermediate matrices in the VECTFIT algorithm and had to be eliminated. Rewriting Equations (2.9) and (2.10) in their modified forms, we get:

$$\mathbf{Z_{h\_fit}}(s) = \mathbf{R_0} + \sum_{k=1}^{K_1} \frac{\mathbf{R_k}}{s - P_k} \tag{3.7}$$

$$\mathbf{Y_{h\_fit}}(s) = \mathbf{G_0} + \sum_{k=1}^{K_2} \frac{\mathbf{G_k}}{s - Q_k} \tag{3.8}$$

Also, for preservation of symmetry, the L-shaped network implementation of the telegrapher's equation as shown in Figure 2.1 has been modified to the π–network topology of Figure 3.3 which can be expressed mathematically by modifying Equation (2.7) to (3.9) and (2.8) to (3.10), respectively. Applying Kirchoff's current and voltage laws to Figure 3.3, we obtain:

$$\mathbf{V}_\Delta(\omega) = \mathbf{V_L}(\omega) - \mathbf{V_R}(\omega) = \mathbf{Z_h}(\omega)\,\mathbf{I}(\omega) \tag{3.9}$$

$$\mathbf{I}_\Delta(\omega) = \mathbf{I_L}(\omega) - \mathbf{I}(\omega) = \mathbf{I}(\omega) - \mathbf{I_R}(\omega) = \frac{\mathbf{Y_h}}{2}(\omega)\,\mathbf{V_L}(\omega) \tag{3.10}$$

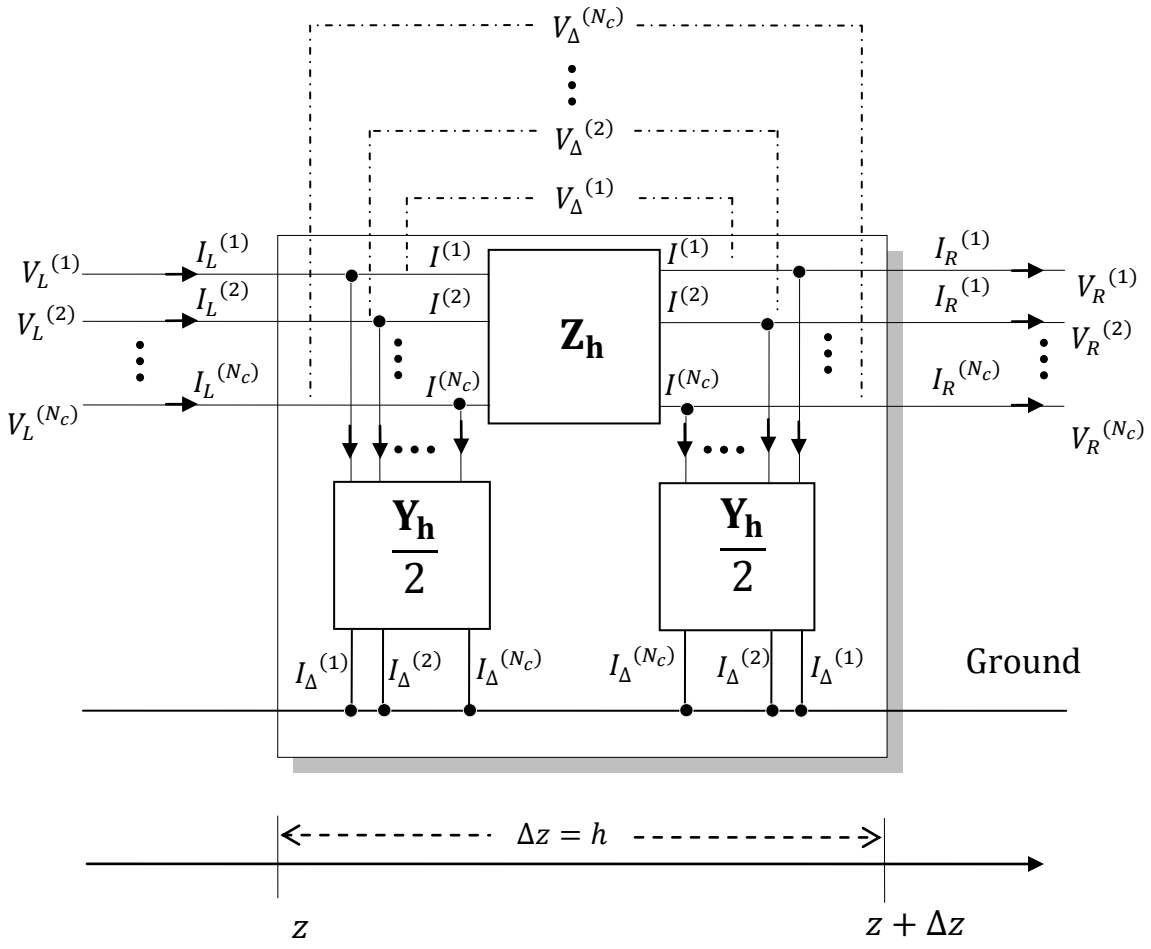

Figure 3.3: π–shaped network topology

Substituting the rational function form of the approximate matrices in place of the actual impedance and admittances matrices, Equations (3.9) and (3.10) can be rewritten in the Laplacian domain as

$$\mathbf{V}_\Delta(s) \cong \mathbf{Z_{h\_fit}}(s)\,\mathbf{I}(s) = \left[\mathbf{R_0} + \sum_{k=1}^{K_1} \frac{\mathbf{R_k}}{s - P_k}\right] \mathbf{I}(s) \tag{3.11}$$

$$\mathbf{I}_\Delta(s) \cong \frac{\mathbf{Y_{h\_fit}}}{2}(s)\,\mathbf{V_L}(s) = \left[\mathbf{G_0} + \sum_{k=1}^{K_2} \frac{\mathbf{G_k}}{s - Q_k}\right] \mathbf{V_L}(s) \tag{3.12}$$

Equations (3.11) and (3.12) can be expressed in the expanded form as:

$$V_{\Delta}{}^{(i)}(s) = \sum_{j=1}^{N} Z_{h\_fit}^{(ij)}(s)\, I^{(j)}(s)$$
$$= \sum_{j=1}^{N} \left\{ R_0{}^{(ij)}(s)\, I^{(j)}(s) \right\} + \sum_{k=1}^{K_1} \left[\left(\frac{1}{s - P_k} \right) \sum_{j=1}^{N} \left\{ R_k^{(ij)} I_j(s) \right\} \right] \tag{3.13}$$

$$I_{\Delta}{}^{(i)}(s) = \sum_{j=1}^{N} \frac{Y_{h\_fit}^{(ij)}}{2}(s)\ V_L{}^{(j)}(s)$$
$$= \sum_{j=1}^{N} \left\{ G_0{}^{(ij)}(s)\, V_L{}^{(j)}(s) \right\} + \sum_{k=1}^{K_2} \left[\left(\frac{1}{s - Q_k} \right) \sum_{j=1}^{N} \left\{ G_k^{(ij)} V_L{}^{(j)}(s) \right\} \right] \tag{3.14}$$

Equations (3.13) and (3.14) can be recast in the form of Equations (3.15) and (3.16).

$$V_{\Delta}{}^{(i)}(s) = V_{\Delta_0}^{(i)} + \sum_{k=1}^{K_1} V_{\Delta_k}^{(i)} \tag{3.15}$$

$$I_{\Delta}{}^{(i)}(s) = I_{\Delta_0}^{(i)} + \sum_{k=1}^{K_2} I_{\Delta_k}^{(i)} \tag{3.16}$$

The circuit analogy of Equations (3.13) and (3.14) is directly deducible by treating their right-hand sides as the algebraic sum of dependent voltages and currents as shown in simplified form in Equations (3.15) and (3.16), respectively.

In Equation (3.13), the term $R_0{}^{(ij)} I_j(s)$ can be treated as a linear voltage-controlled voltage source. The controlling voltage would be the voltage across a resistance of $1\,\Omega$ driven by a current source $I_j(s)$ of amplitude $R_0{}^{(ij)}$. By analogy, the term $G_0{}^{(ij)}(s)\, V_L{}^{(j)}(s)$ in Equation (3.14) can be thought of as a linear current-controlled current source with the controlling current being the current through a conductance of

$1\ \Omega^{-1}$ with a voltage source $V_j(s)$ of amplitude ${G_0}^{(ij)}$ connected across it. The circuit representation of the constant terms is shown in Figure 3.4.

Each real pole term in (3.13) can be considered as a linear voltage-controlled voltage-source with the controlling voltage being the voltage across a parallel combination of a resistance of value $-1/P_k\ \Omega$ and a capacitance of value 1 F driven by a current source $I_j(s)$ of amplitude $R_k^{(ij)}$. Again by analogy, each real pole term in (3.14) can be considered a linear current-controlled current-source with the controlling current being the current through a series combination of a resistance of value $-P_k\ \Omega$ and an inductance of value 1 H with a voltage source $V_j(s)$ of amplitude $G_k^{(ij)}$connected across the combination. The circuit representation of the real terms with real poles is shown in Figure 3.5.

The circuit diagrams for the matrices $\mathbf{Z_{h\_fit}}$ and $\mathbf{Y_{h\_fit}}/2$ are shown in Figures 3.6 and 3.7, respectively.

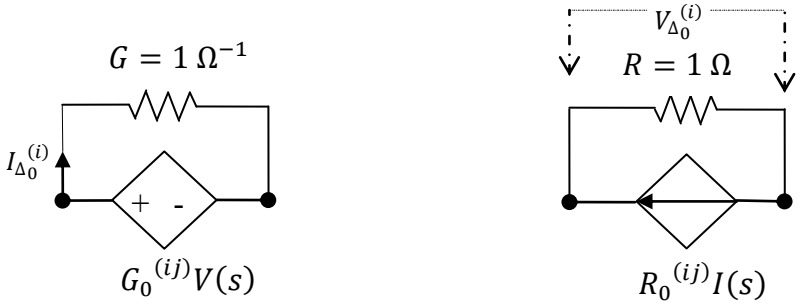

Figure 3.4: The circuit representation of the constant terms

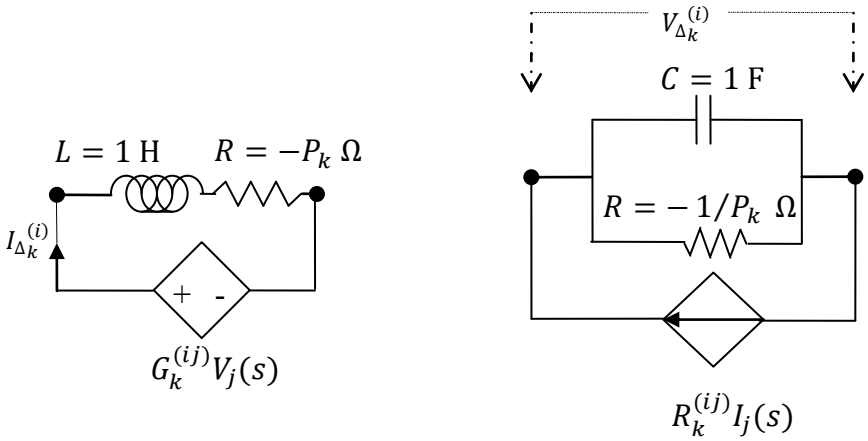

Figure 3.5: The circuit representation of the terms with the real poles

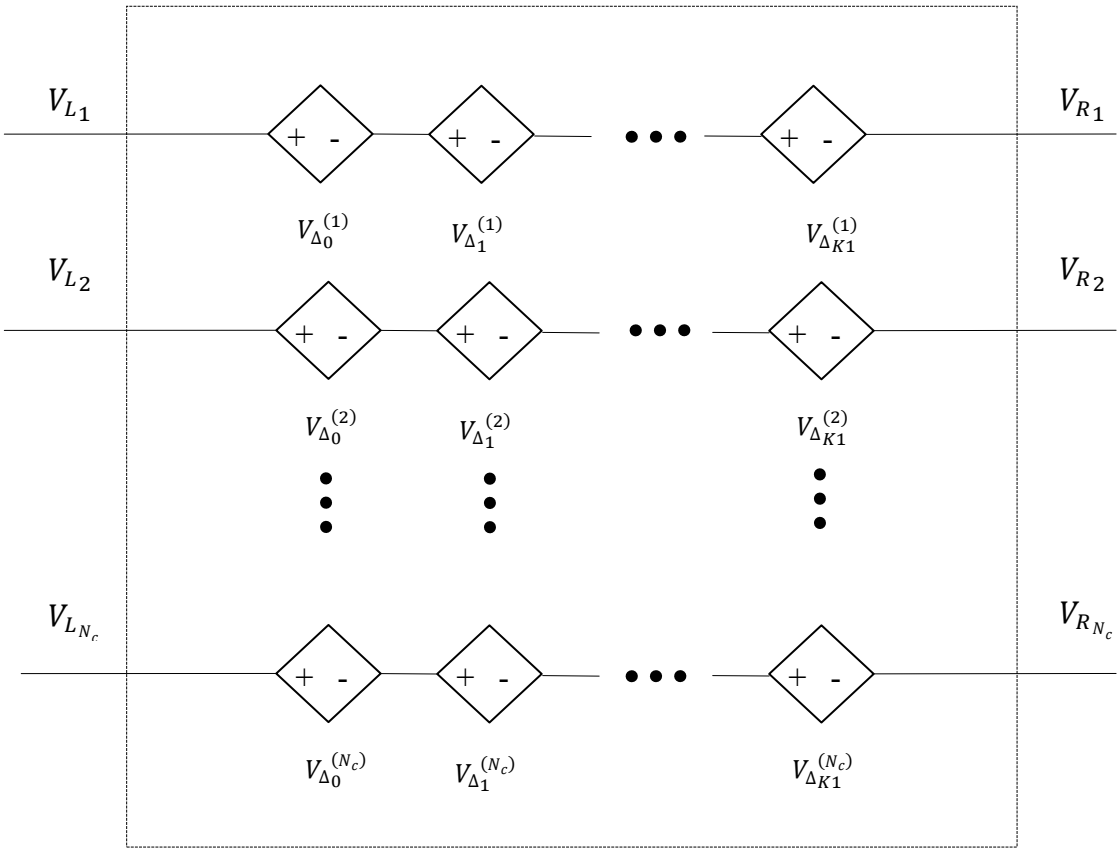

Figure 3.6: Circuit diagram for the $\mathbf{Z_h}$ element

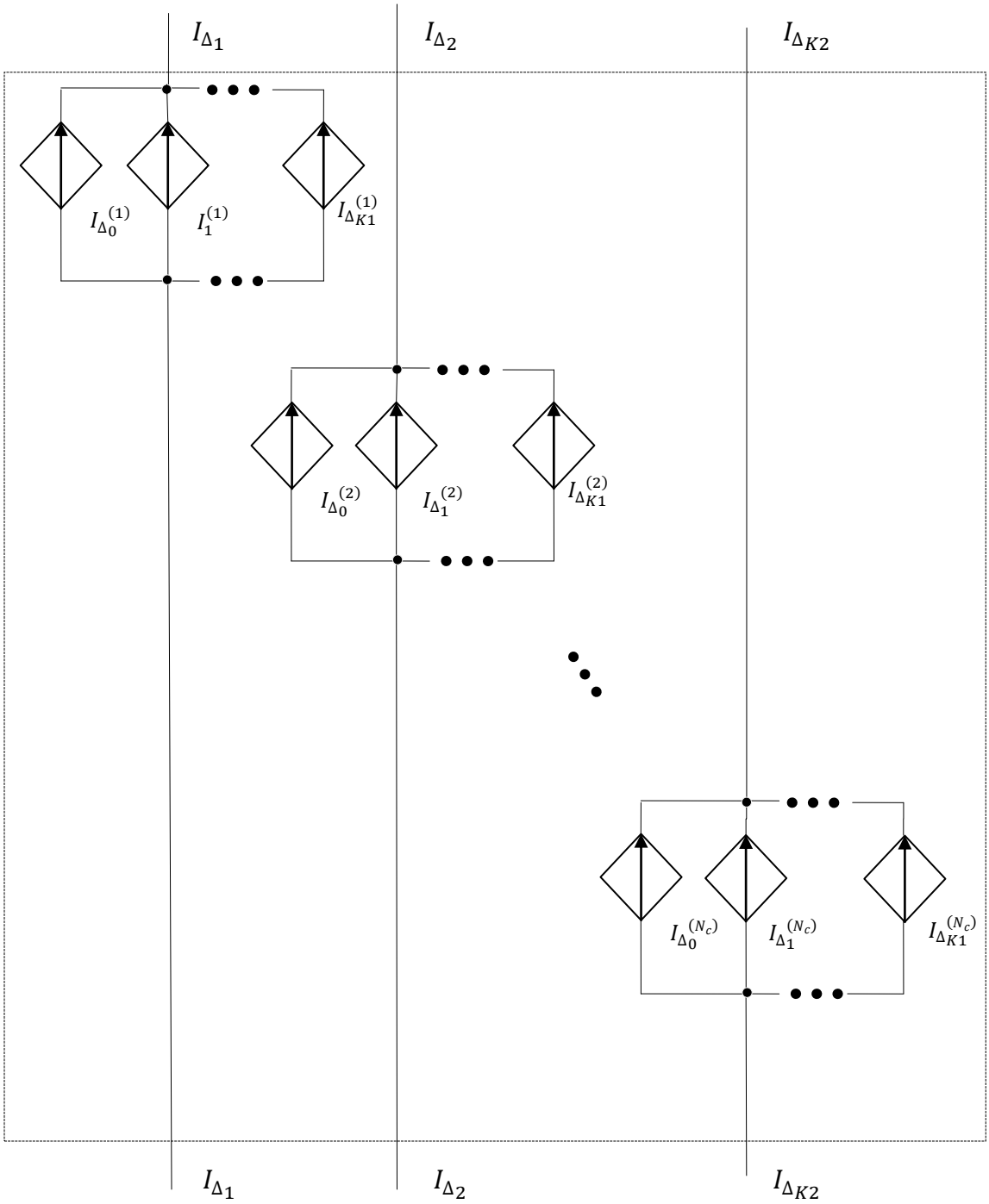

Figure 3.7: Circuit diagram for $\boldsymbol{Y_{h\_fit}}/2$ element

A simplified π–network topology representation of each segment of the transmission line is shown in Figure 3.8.

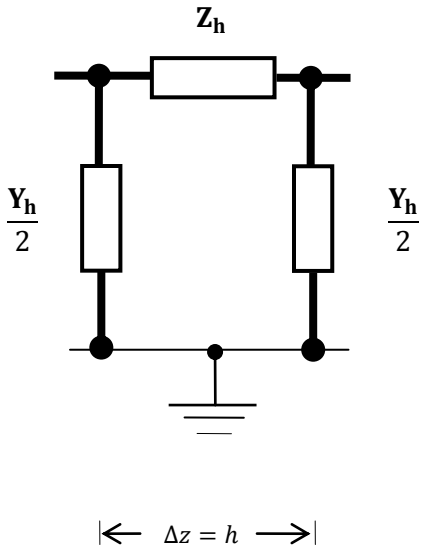

Figure 3.8: π–block, the building block of the line

CHAPTER 4

NUMERICAL SIMULATIONS

4.1 Introduction

This section demonstrates the application of the developed methodology through some practical examples. The first example shows the incorporation of a section of a micro-strip line into a popular commercial circuit simulator, HSPICE, the transmission line parameters of which are extracted using UIUC2D, a two-dimensional RLCG extractor. The quarter wavelength lumped approximation used as an upper bound for the choice of the maximum possible segment length is established through a numerical example. The methodology is validated by comparing the analytical model of a lossy transmission line obtained from transmission line theory with the W-element feature available in HSPICE. To compare the computational efficiency of the proposed methodology with that of the previous approach, transient analysis is performed on the MTL models generated through each approach for a three-conductor interconnect example. The accuracy of the two approaches is then compared by measuring the Y-parameter results of both models. Tests are also performed to ascertain whether increasing the number of segments has any effect on the transient simulations. All the simulations were run on a Windows Vista platform running on an Intel Core 2 Duo CPU T9300 processor clocked at 2.50 GHz with 3 GB RAM.

4.2 The Micro-Strip Line

The cross-sectional view of the uniform micro-strip line is shown in Figure 4.1. The length of the micro-strip line structure was arbitrarily chosen as 40 cm. The

methodology has been elaborated sequentially with simulation results.

4.2.1 Using UIUC2D to generate the p.u.l. impedance and admittance matrices

The transmission line parameters of the micro strip line were obtained from UIUC2D field solver software. UIUC2D has two choices for frequency sweep: quadratic and linear. Linear sweep keeps the difference between successive frequencies constant (i.e. $\omega(n+1) - \omega(n) = \text{constant}$) while quadratic keeps the square root of the difference as constant (i.e. $\sqrt{\omega(n+1) - \omega(n)}$ = constant), where $\omega(n)$ is the *n*th frequency point in the frequency sweep. For the purposes of our application, i.e., the generation of an equivalent circuit, the quadratic sweep was the recommended choice [17].

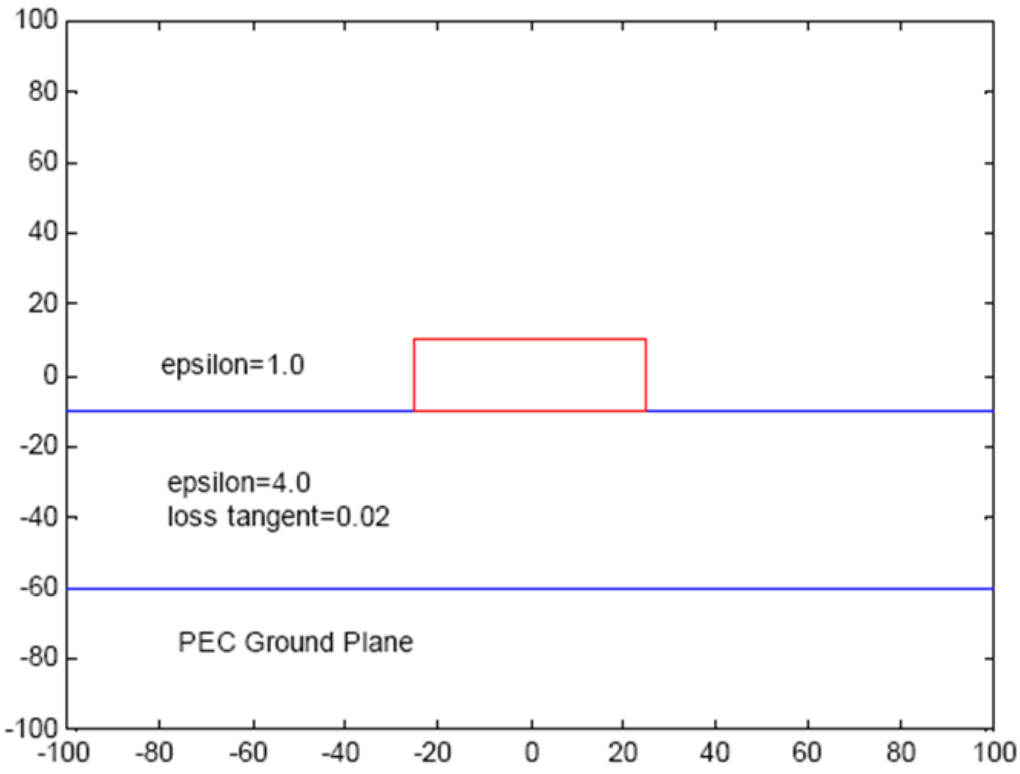

Figure 4.1: Micro-strip line: Distances are in microns

The quadratic frequency sweep was performed from 1 MHz to 10 GHz for a total of 20 frequency points. As a result, the frequency-dependent per unit length inductance $\left[\mathbf{L_{pul}}(\omega)\right]$, capacitance $\left[\mathbf{C_{pul}}(\omega)\right]$, resistance $\left[\mathbf{R_{pul}}(\omega)\right]$, and conductance $\left[\mathbf{G_{pul}}(\omega)\right]$ matrices were obtained for a total of 20 frequency points. The impedance and admittance matrices $\left[\mathbf{Z_{pul}}(\omega)\right]_{(1\times 1\times 20)}$ and $\left[\mathbf{Y_{pul}}(\omega)\right]_{(1\times 1\times 20)}$ can then be written as:

$$\mathbf{Z_{pul}}(\omega) = \mathbf{R_{pul}}(\omega) + j\omega\, \mathbf{L_{pul}}(\omega) \tag{4.1}$$

$$\mathbf{Y_{pul}}(\omega) = \mathbf{G_{pul}}(\omega) + j\omega\, \mathbf{C_{pul}}(\omega) \tag{4.2}$$

4.2.2 Calculating the maximum permissible segment length

The uniform transmission line of length L was divided into segments of equal length, as shown in Figure 4.2. The length h was chosen so as not to exceed h_{max}, the maximum permissible length for lumped approximation. The optimal length for h_{max} was predetermined from trial-and-error experiments to be a quarter wavelength. The process of determining this length entailed performing HSPICE network analysis on the transmission line model of the micro-strip line obtained using the π-network topology and then observing the Y-parameters for different fractions of the smallest wavelength. It was found that the smallest wavelength (λ_{min}) corresponds to the highest frequency of the bandwidth of interest as shown in Table 4.1. Also, for qualitative reasons, transient analysis was subsequently performed to find out the effects of choosing h_{max} as a quarter of the smallest wavelength (i.e. $h < h_{max} = \lambda_{min}/4$) on the quality of signal propagation over the transmission line. This process of determining h_{max} has been explained in detail in Section 4.3.

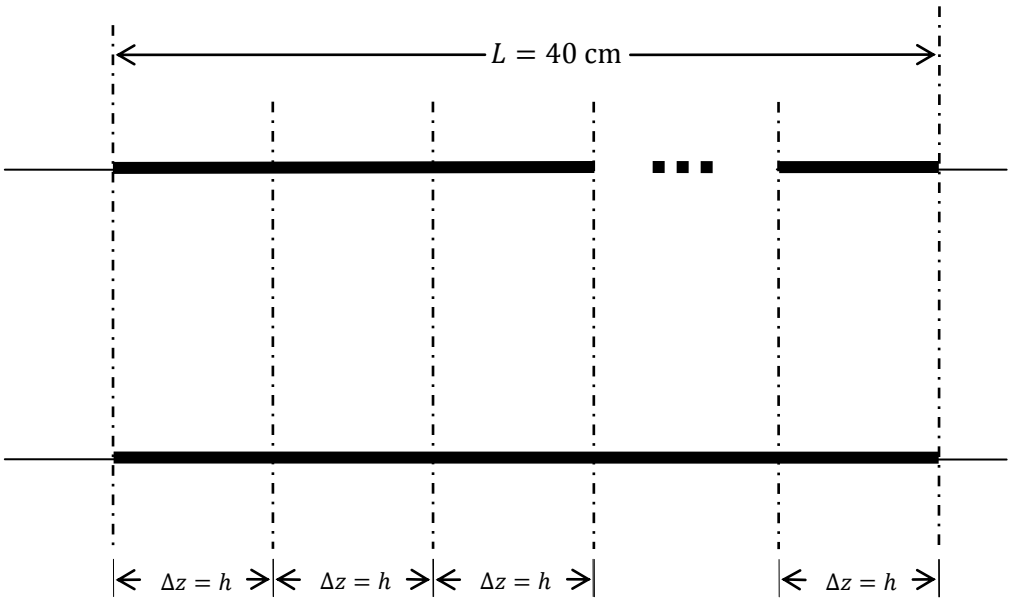

$$h = \frac{L}{\left\lceil \frac{L}{h_{max}} \right\rceil} = 0.45455 < h_{max} = 0.25\,\lambda_{min} = 0.25 \times 1.8256 = \ 0.45639 \text{ cm}$$

$$L = h\,\left\lceil \frac{L}{h_{max}} \right\rceil = 0.45455 \times 88 \text{ cm} = 40 \text{ cm}$$

Figure 4.2: Micro-strip line of length L = 40 cm

For the case of the micro-strip line in Figure 4.1, the maximum allowable length was found to be 0.45639 cm for the highest frequency of bandwidth. This was based on wavelength calculation from the velocity data provided by UIUC2D for different frequencies. It was found that it would require 88 equal length sections to be daisy-chained together to represent the given transmission line 40 cm long. The data generated by UIUC2D is tabulated in Table 4.1.

Table 4.1: Delay, velocity and attenuation values generated by UIUC2D

freq (GHz)	Delay (sec/m)	Velocity (m/sec)	Attenua-tion(dB/m)	λ (m)
0.001	5.45E-09	8.75E+07	0.546	87.512
0.029	5.45E-09	1.71E+08	1.224	5.941
0.112	5.45E-09	1.75E+08	1.989	1.563
0.250	5.45E-09	1.77E+08	3.135	0.708
0.444	5.45E-09	1.79E+08	4.445	0.402
0.694	5.45E-09	1.80E+08	5.800	0.259
0.998	5.45E-09	1.80E+08	7.369	0.181
1.358	5.45E-09	1.81E+08	9.061	0.133
1.774	5.45E-09	1.81E+08	10.858	0.102
2.245	5.45E-09	1.81E+08	12.791	0.081
2.771	5.45E-09	1.82E+08	14.859	0.066
3.353	5.45E-09	1.82E+08	17.066	0.054
3.990	5.45E-09	1.82E+08	19.403	0.046
4.682	5.45E-09	1.82E+08	21.879	0.039
5.430	5.45E-09	1.82E+08	24.487	0.034
6.233	5.45E-09	1.82E+08	27.226	0.029
7.092	5.45E-09	1.82E+08	30.104	0.026
8.006	5.45E-09	1.82E+08	33.112	0.023
8.975	5.45E-09	1.83E+08	36.238	0.020
10.000	5.45E-09	1.83E+08	39.467	0.018

4.2.3 Applying the VECTFIT algorithm

The impedance and admittance matrices for the section of transmission line of length *h* were approximated as follows:

$$\mathbf{Z_h}(\omega) \triangleq h\, \mathbf{Z_{pul}}(\omega) \tag{4.3}$$

$$\mathbf{Y_h}(\omega) \triangleq h\, \mathbf{Y_{pul}}(\omega) \tag{4.4}$$

The $\mathbf{Z_h}(\omega)$ and $\mathbf{Y_h}(\omega)$ matrices were fitted independently with a common set of poles for each matrix using matrix fitting software [13]. After experimenting with the parameters of the VECTFIT software it was found out that the best fit was obtained by selecting four poles with the same order for the numerator and denominator of the

rational function. This small order of approximation was possible because the length of the transmission line segment was smaller than the smallest wavelength in the frequency spectrum of interest. Parameters of VECTFIT were further chosen in a way such that the generated poles were stable. VECTFIT ensures this by flipping the unstable poles to the left half-plane poles. The final forms of the rational function approximation in the Laplacian domain for the admittance and impedance matrices were obtained as follows:

$$\mathbf{Z_h}(s) = \mathbf{R_0} + \sum_{k=1}^{4} \frac{\mathbf{R_k}}{s - P_k} \tag{4.5}$$

$$\mathbf{Y_h}(s) = \mathbf{G_0} + \sum_{k=1}^{4} \frac{\mathbf{G_k}}{s - Q_k} \tag{4.6}$$

The results of the VECTFIT are shown in Figures 4.3-4.6. It can be seen from the plots that there is a close conformation between the elements of the matrices generated by UIUC2D and their rational function approximation generated by VECTFIT.

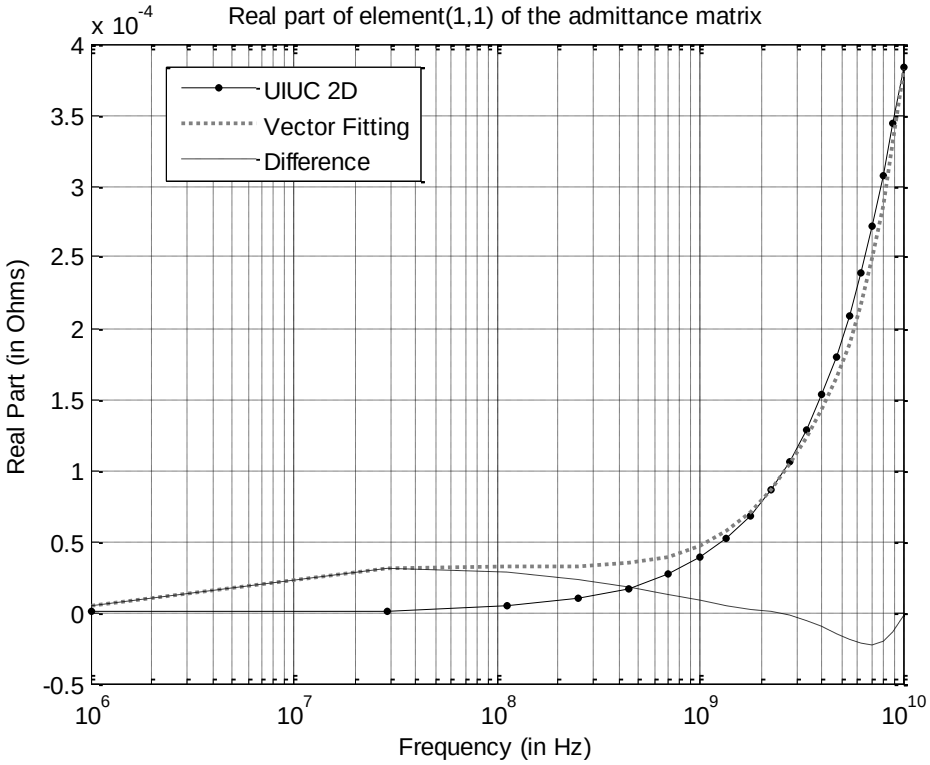

Figure 4.3: Comparison of the plots of Re $\left[\boldsymbol{Y_h}^{(1,1)}\right]$

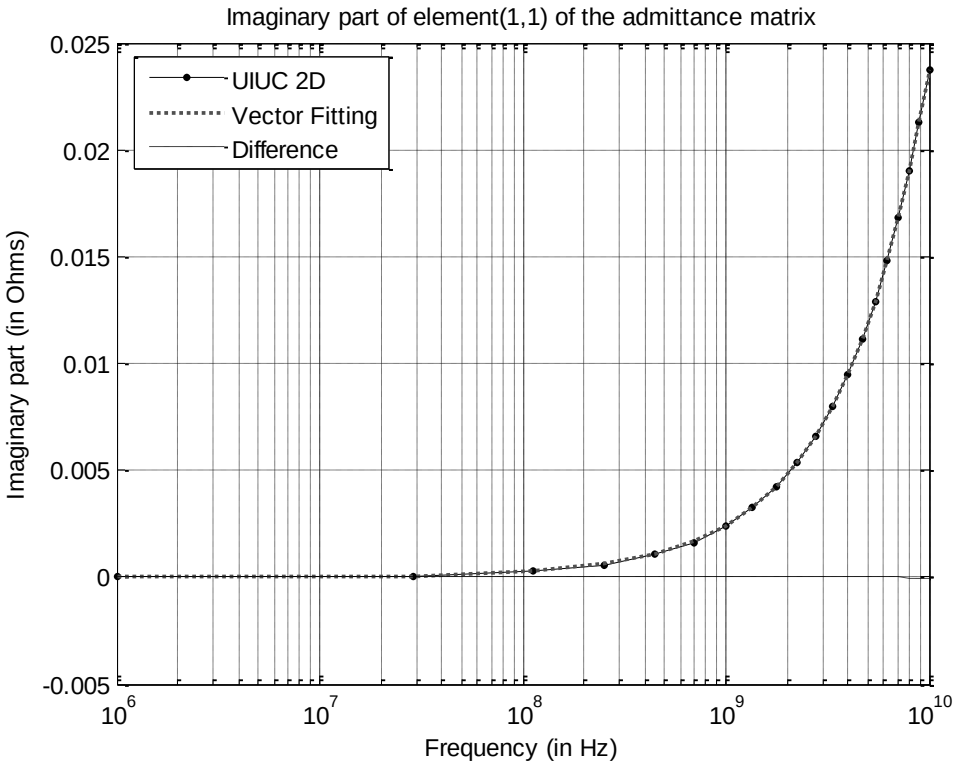

Figure 4.4: Comparison of the plots of Im $\left[\boldsymbol{Y_h}^{(1,1)}\right]$

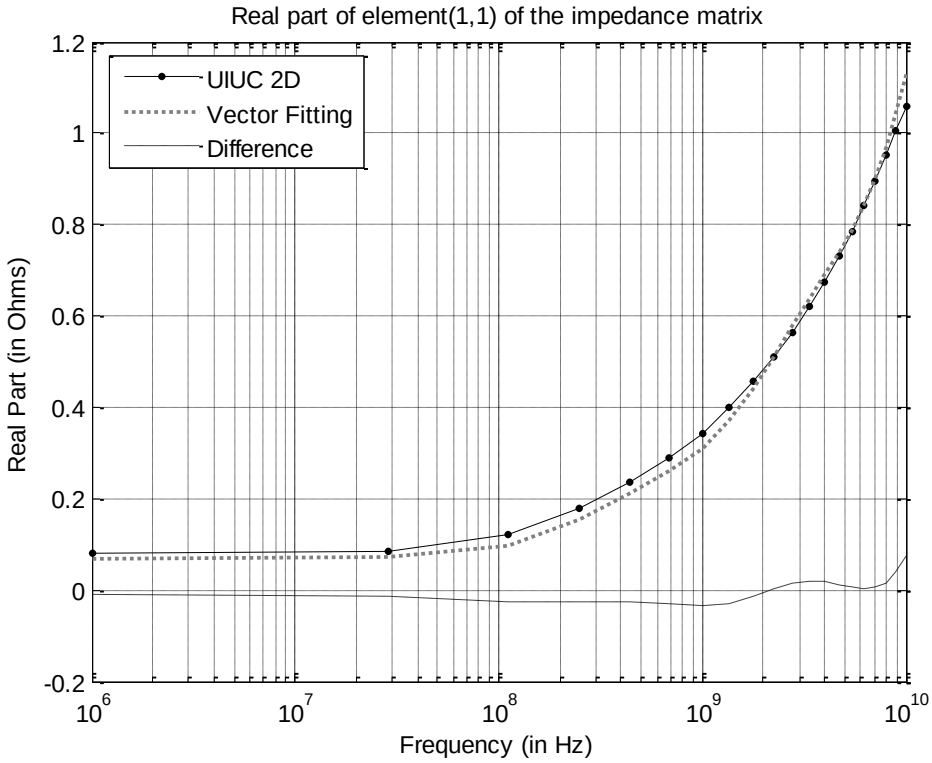

Figure 4.5: Comparison of the plots of Re $\left[\boldsymbol{Z_h}^{(1,1)}\right]$

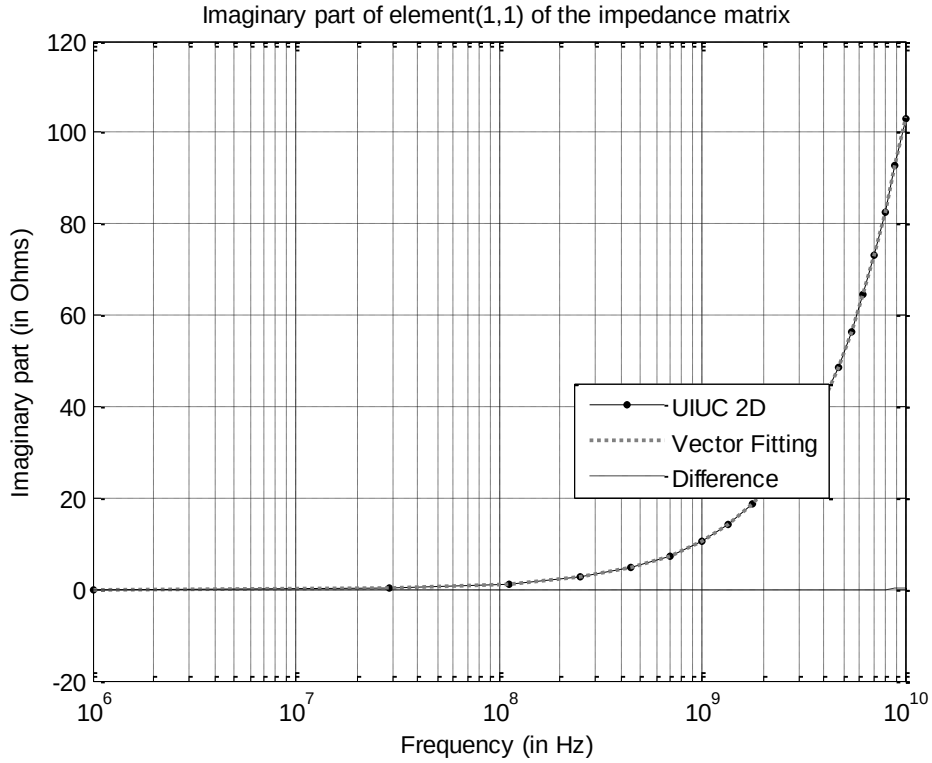

Figure 4.6: Comparison of the plots of Im $\left[\boldsymbol{Z_h}^{(1,1)}\right]$

4.2.4 Equivalent circuit generation

The rational function forms of admittance and impedance matrices available in Section 4.2.3 are ideal for synthesizing a passive circuit representation for HSPICE. A detailed description of this procedure is available in Chapter 3. The $\mathbf{Z_h}(\omega)$ and $\mathbf{Y_h}(\omega)$ matrices in their HSPICE implementations could be effectively arranged to approximate the behavior of our original line as shown in Figure 4.7. The part of the circuit between the vertical dotted lines is the circuit representation for the approximated segment of the transmission line which is cascaded together k times so that $L = kh$, where k is an integer denoting the number of segments.

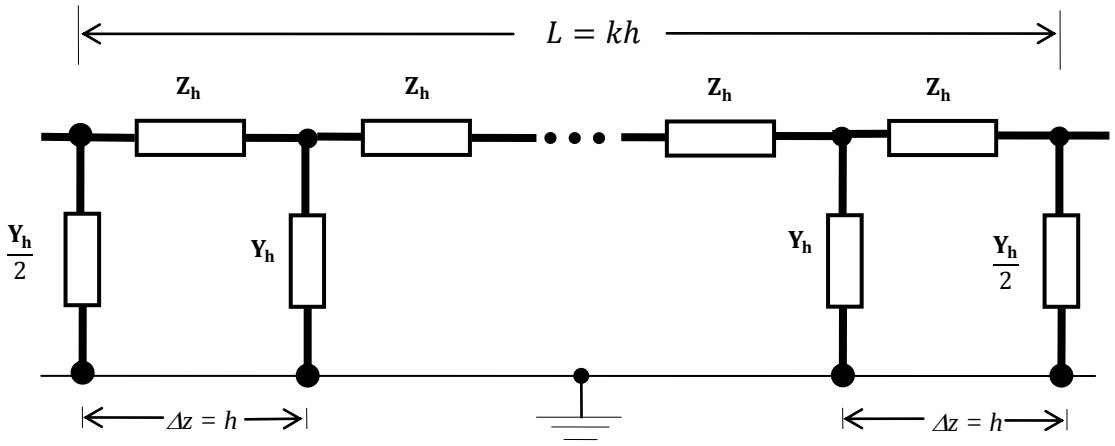

Figure 4.7: π – topology cascaded representation of the segments

Figure 4.8 shows the HSPICE transient simulation results of signal propagation across the transmission line model for a certain length ($L = 40$ cm) of the micro-strip line. A pulse generator with $50\ \Omega$ source resistance sends periodic trapezoidal clock pulses of width 2 ns with 50% duty cycle and 0.2 ns rise and fall times across the transmission line terminated by a $50\ \Omega$ load. It should be noted that the simulation results

were not affected by the choice of line segment length as described in Section 4.2.2, as long as the approximation criterion (i.e., $h < h_{max} = 0.25\ \lambda_{min}$) is satisfied.

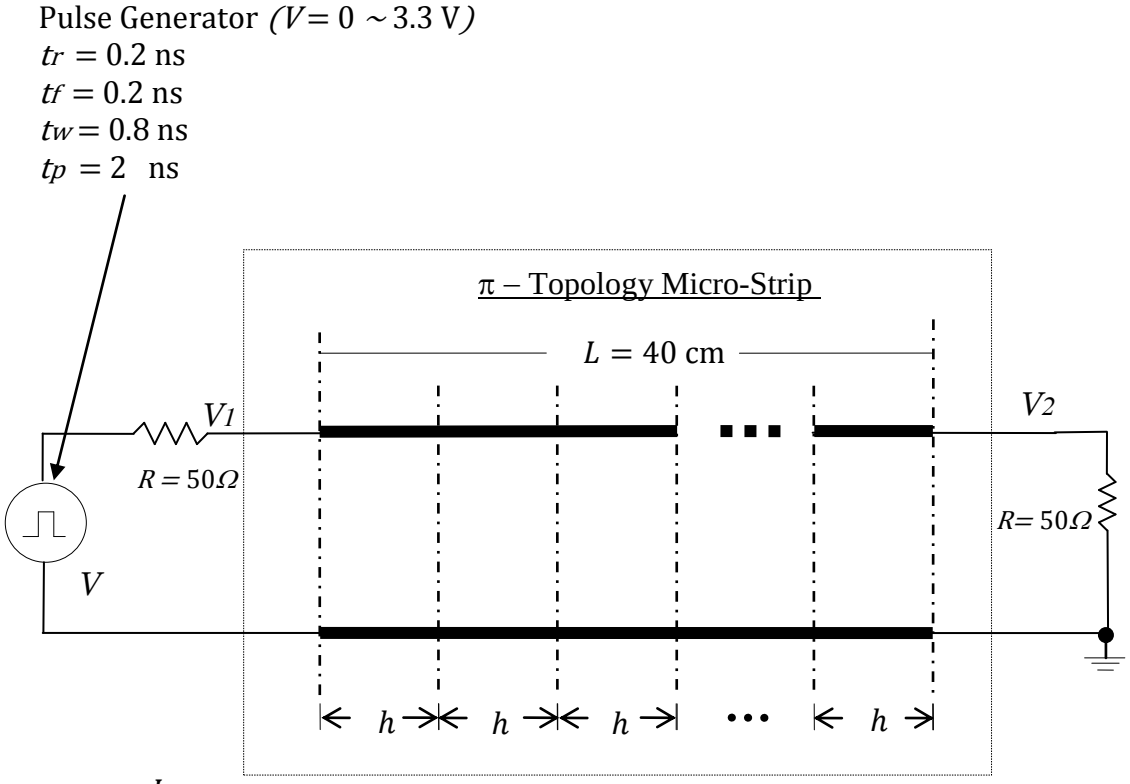

$$h = \frac{L}{\left\lceil \frac{L}{h_{max}} \right\rceil} = 0.45455 < h_{max} = 0.25\ \lambda_{min} = 0.25 \times 1.8256 = 0.45639 \text{ cm}$$

$$L = h \left\lceil \frac{L}{h_{max}} \right\rceil = 0.45455 \times 88 \text{ cm} = 40 \text{ cm}$$

Figure 4.8: Circuit used to for transient plots

Figure 4.9 shows the HSPICE simulation plots of the transient analysis. For delay calculation, the reference voltage values were observed at half the height of the pulse to overcome the difficulties in measurement due to dispersion. The delay encountered by the signal to traverse the length of the transmission line is found from Figure 4.9 to be

$$\Delta t = t_1 - t_2 = 2.45\text{e-}009\text{s} - 2\text{e-}010\text{s} = 2.25 \text{ ns} \quad (4.7)$$

where the values $t_1 = 2e\text{-}010s$ and $t_2 = 2.45e\text{-}009s$ have been taken from Figures

4.9 (a) and 4.9 (c), respectively.

The interaction between the forward-going wave and the returning wave can be seen occurring after 4.1 ns in Figure 4.9 (b). For the trapezoidal pulse train generated by the source in this example, the frequency bandwidth requirements are $f_{min} = 1/\tau =$ 5 GHz, where $\tau = t_r = 0.2$ ns, which falls within the bandwidth spectrum considered for macro-modeling [1]. The Fourier series representation of the periodic pulse train is given as:

$$v(t) = a_0 + \sum_{n=1}^{\infty} a_n cos\left(\frac{2\pi n}{T} t\right) \tag{4.8}$$

where $T = tp =$ pulse-width $= 2$ ns.

The frequency of the first harmonic can be calculated from Equation (4.8) as:

$$f_1 = \frac{2\pi \times 1}{2\pi \times 2 \times 10^{-9}} = 500 \text{ MHz} \tag{4.9}$$

The group velocity of the wave-packet can be calculated from the simulation data obtained from Figure 4.9 to be

$$v_g = \frac{L}{\Delta t} = \frac{0.4}{2.25 \times 10^{-9}} = 1.778 \times 10^8 \, {}^{\text{m}}/_{\text{s}} \approx 1.79 \times 10^8 \, {}^{\text{m}}/_{\text{s}} \tag{4.10}$$

where L is the length of the line and Δt is the time of flight of the pulse.

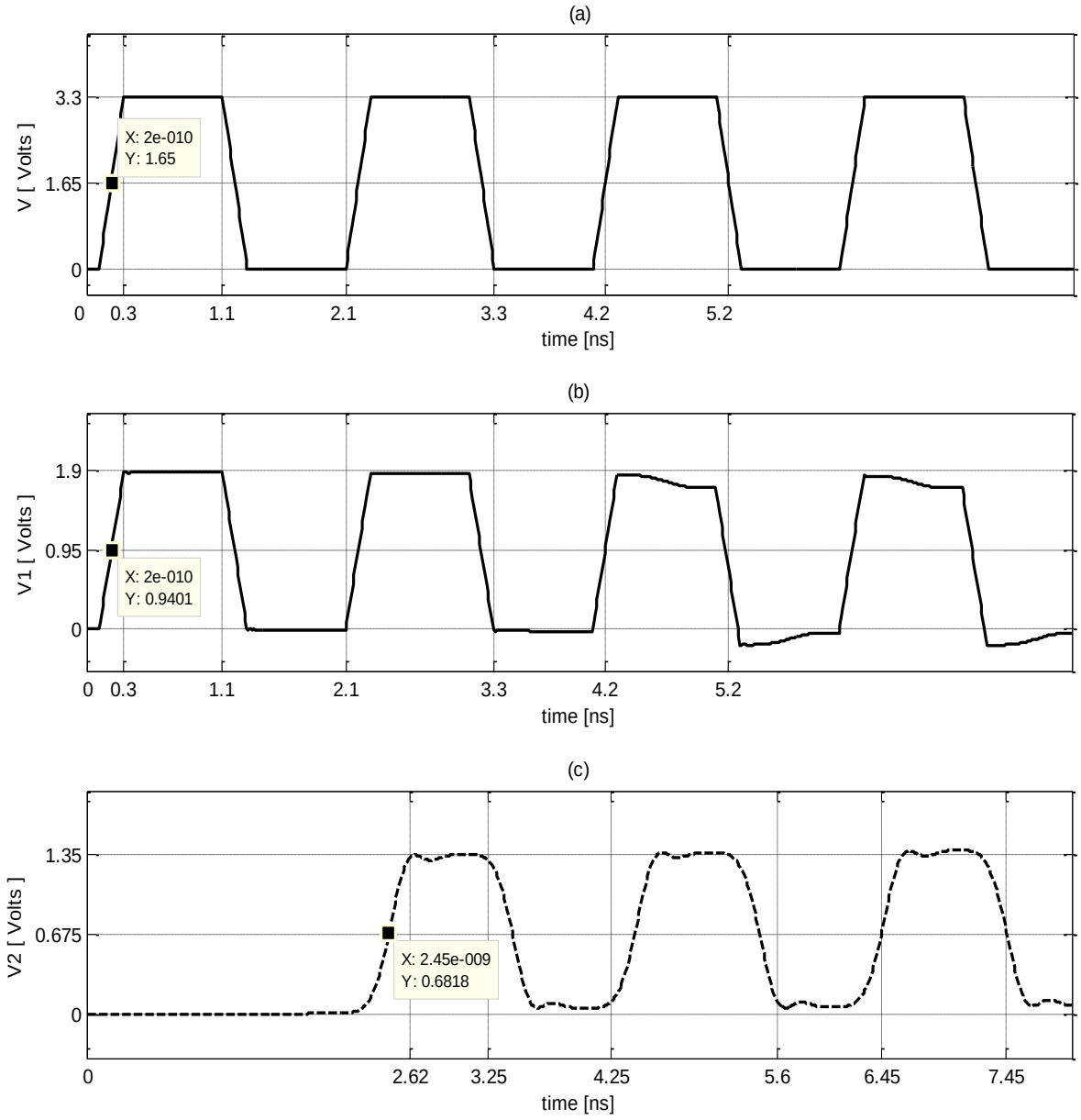

$$\Delta t = t_1 - t_2 = 2.45\text{e-}009\text{s} - 2\text{e-}010\text{s} = 2.25\ \text{ns}$$

$$v_g = \frac{L}{\Delta t} = \frac{0.4}{2.25 \times 10^{-9}} = 1.778 \times 10^8\ \text{m/s} \approx 1.79 \times 10^8\ \text{m/s}$$

Figure 4.9: (a) Voltage V, (b) Voltage V_1, (c) Voltage V_2 of circuit in Figure 4.8

The value of group velocity v_g in Equation (4.10) obtained from HSPICE simulations agrees with the value predicted by UIUC2D. Figure 4.10 is a plot of the frequency vs. speed of propagation data generated by UIUC2D and tabulated in Table 4.1. It can be seen from Figure 4.9 that the interpolated value of $v_g = 1.79 \times 10^8$ m/s corresponding to the value of frequency $f = 500$ MHz, represented as $8.99\ (= log_{10}[5 \times 10^8])$ on the x-axis, is in agreement with the velocity of propagation of the first harmonic frequency calculated from transient analysis plots in Equation (4.10). In other words, $v_p(f = 500\text{ MHz}) = 1.79 \times 10^8$ m/s (from UIUC2D) $= v_g$ (from transient simulation plot in Figure 4.9).

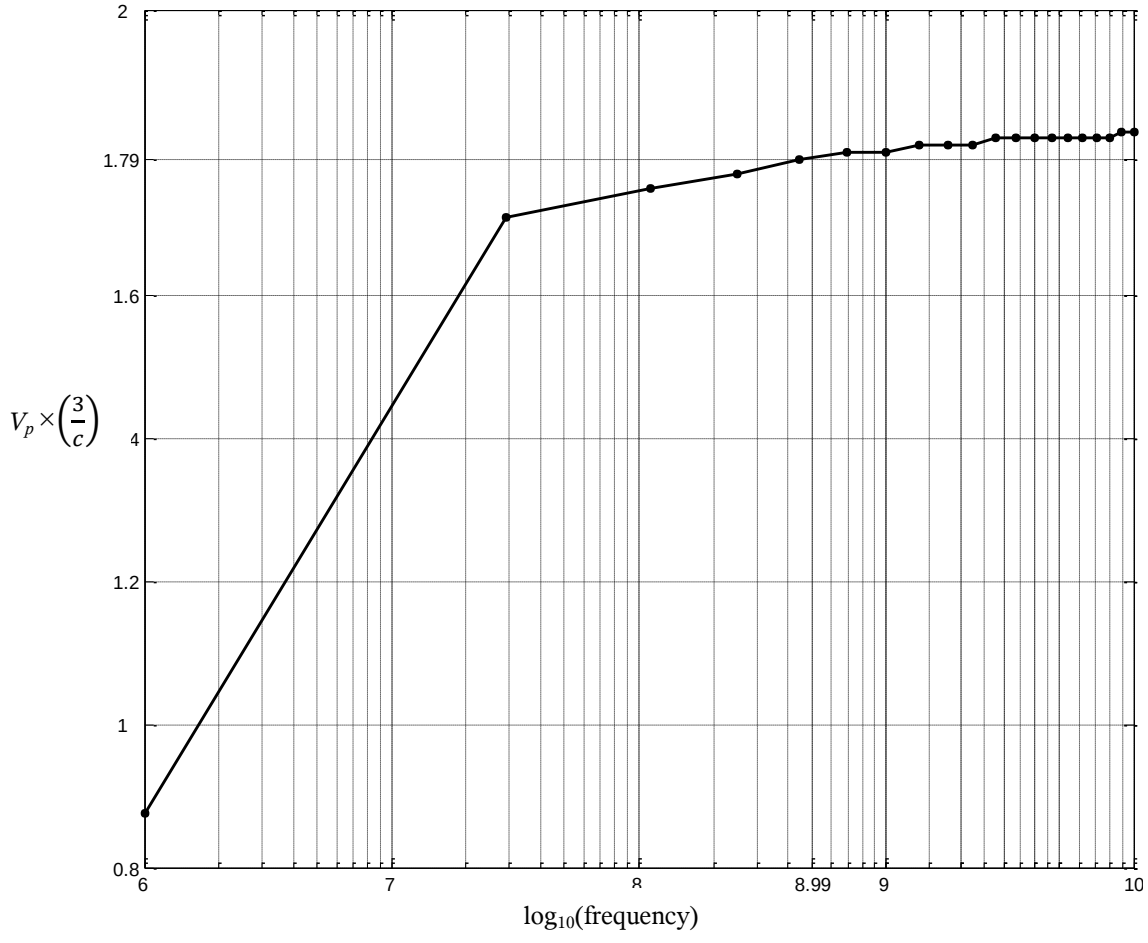

Figure 4.10: Speed of propagation vs. frequency (from Table 4.1)

4.3 Establishing the Quarter Wavelength Lumped Approximation Criterion

The upper bound for maximum allowable transmission line segment *(h_{max})* was determined after performing network analysis on the π-network micro-strip line model as shown in Figure 4.11.

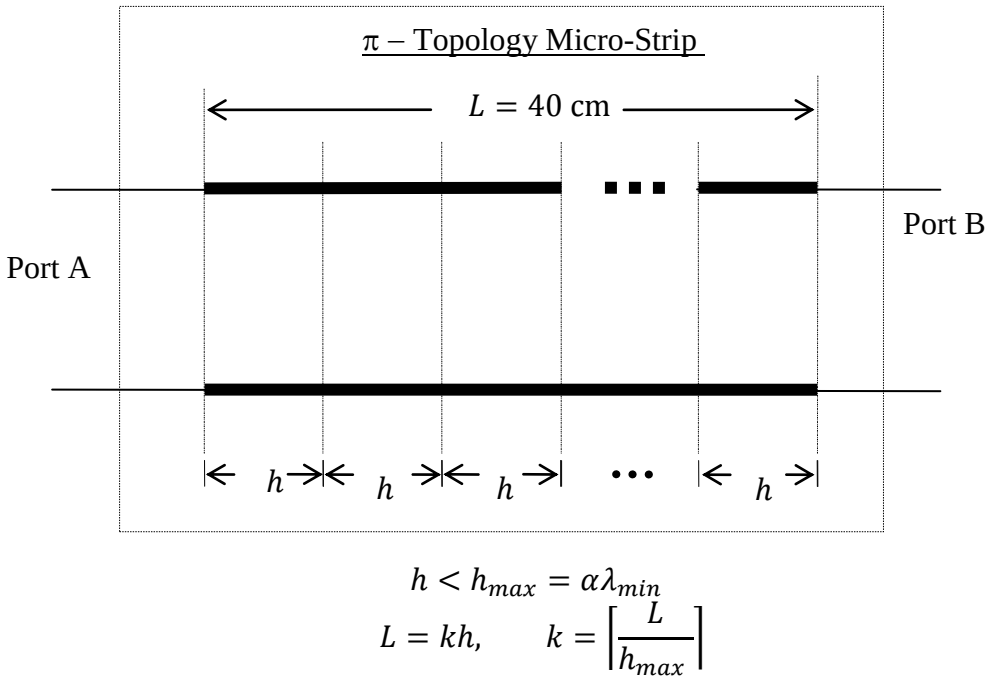

Figure 4.11: Circuit used for two-port network analysis

Because of reciprocity, the analytical expressions of the diagonal and off-diagonal elements of the admittance matrix of the two-port network are the same, i.e., $Y_{11} = Y_{22}$ and $Y_{12} = Y_{21}$. The process was repeated for several different values of $h_{max} = \alpha\lambda_{min}$ for $\alpha = {}^{1}/_{2}, {}^{1}/_{2.5}, {}^{1}/_{3}, {}^{1}/_{4}, {}^{1}/_{5}, {}^{1}/_{7}$ and ${}^{1}/_{10}$. It should be noted that in all these trials only α was changed and all other parameters including the number of poles used for fitting ($N = 4$) were kept constant. Plots of Y_{11} and Y_{12} were obtained for different values of α and it was qualitatively observed that $\alpha = {}^{1}/_{4}$ provided the best value of

approximation in terms of trade-off between accuracy and computational efficiency. Figures 4.12 and 4.13 show the Y_{11} and Y_{21} parameters of the transmission line models for lumped approximation values of h_{max} equal to $\lambda_{min}/4$ and $\lambda_{min}/10$, respectively. It can be clearly observed that the deviation of the Y-parameters of the line for the overkill value of $\alpha = {}^{1}/_{10}$ to yield $h_{max} = \lambda_{min}/10$ from that of $h_{max} = \lambda_{min}/4$ is quite insignificant.

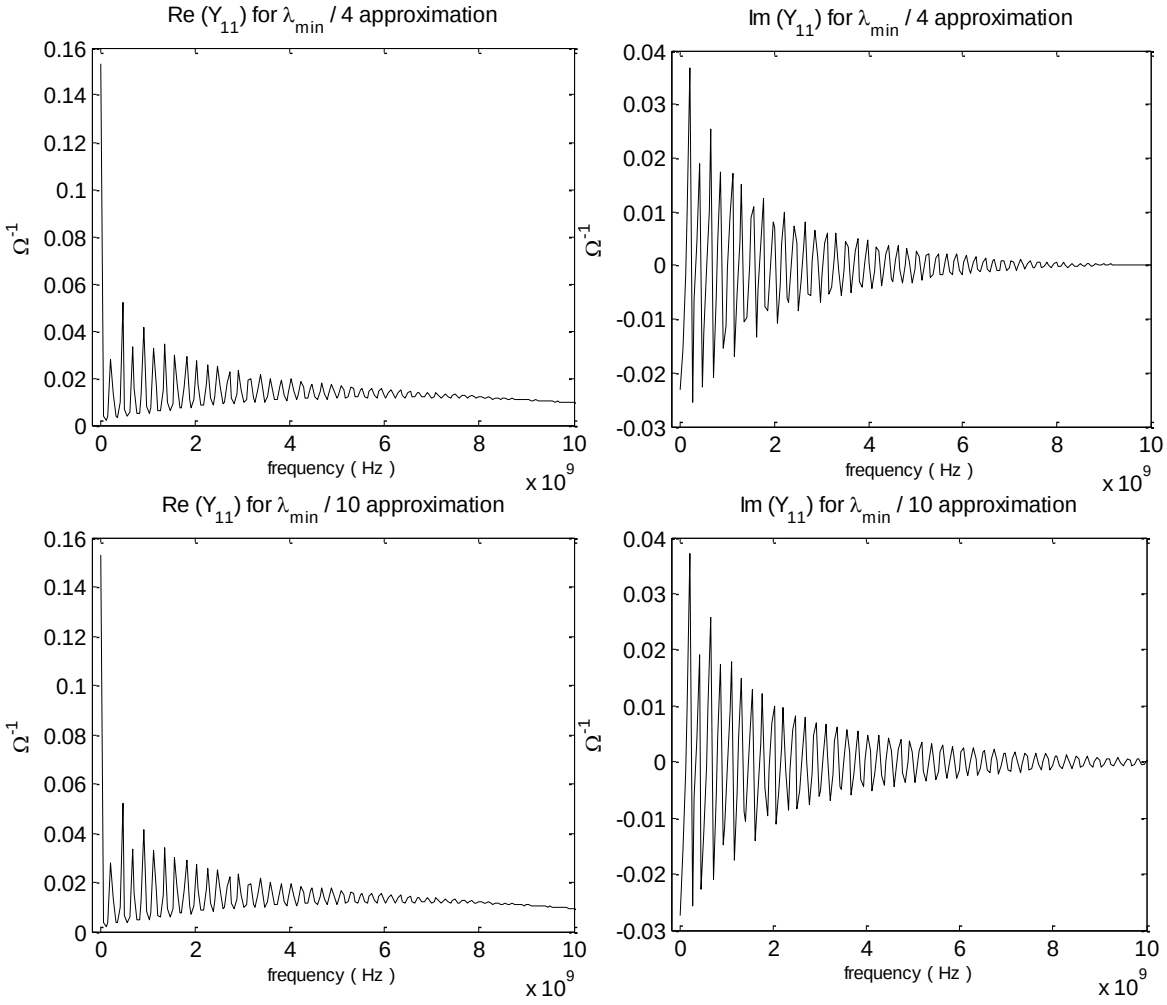

Figure 4.12: Comparison of Y_{11} (or Y_{22}) parameters for $\lambda_{min}/4$ and $\lambda_{min}/10$ approximations

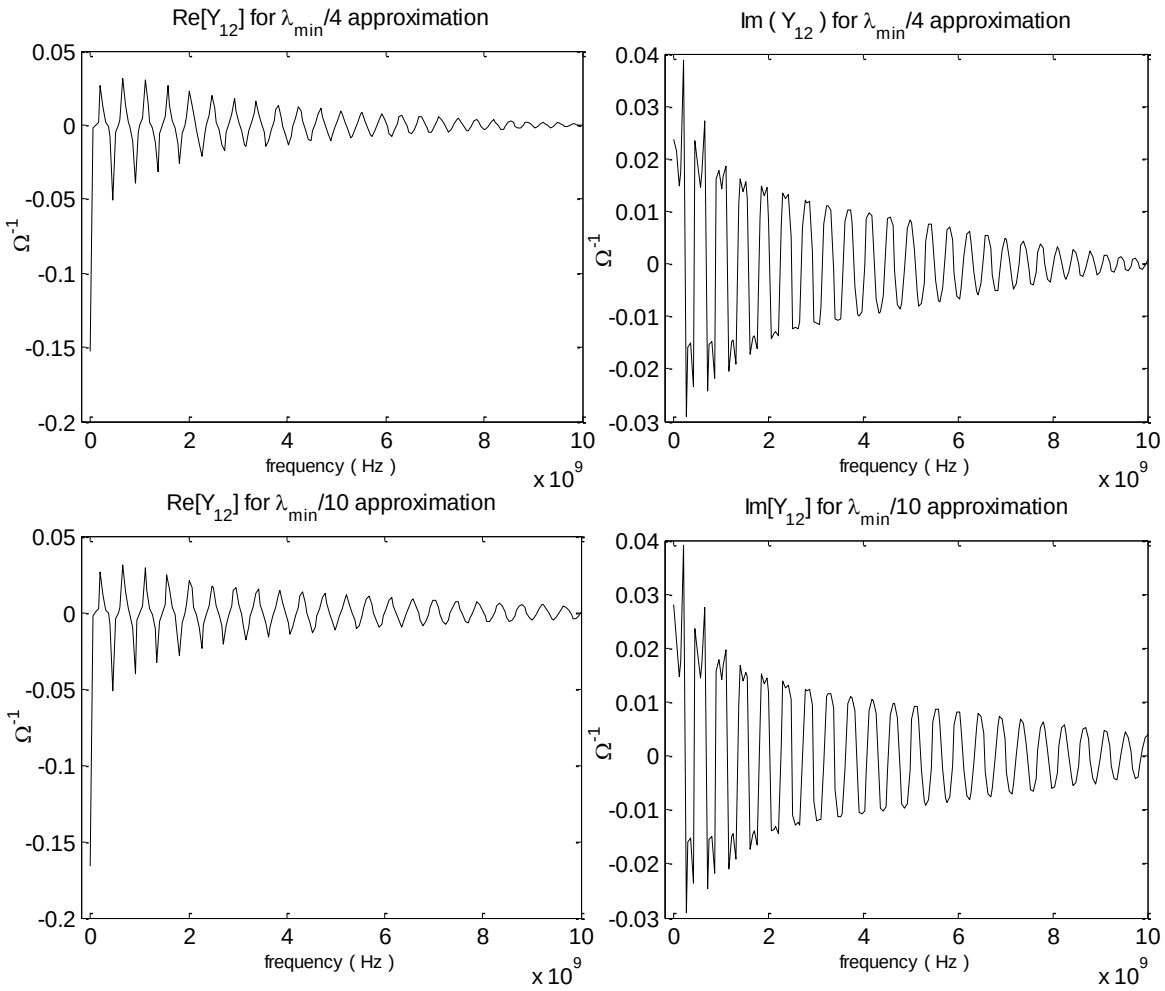

Figure 4.13: Comparison of Y_{12} (or Y_{21}) parameters for $\lambda_{min}/4$ and $\lambda_{min}/10$ approximations

Using the circuit in Figure 4.14, transient analysis was also performed for different values of h_{max} to further corroborate the process of choosing the optimal value of α. Figure 4.15 shows a snapshot of the transient analysis performed on the transmission line models with lumped approximation values of h_{max} equal to $\lambda_{min}/4$ and $\lambda_{min}/10$, respectively.

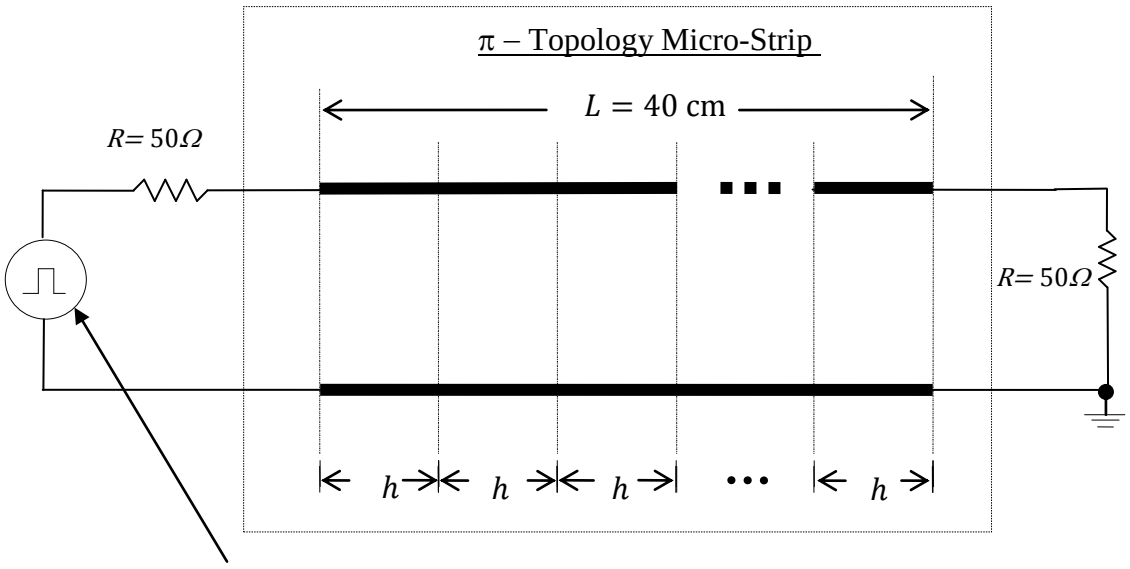

Pulse Generator ($V = 0 \sim 3.3$ V)
$t_r = 0.2$ ns
$t_f = 0.2$ ns
$t_w = 0.8$ ns
$t_p = 2$ ns

$$h < h_{max} = \alpha\lambda_{min}$$
$$L = kh, k = \left\lceil \frac{L}{h_{max}} \right\rceil$$

Figure 4.14: Circuit used for transient analysis

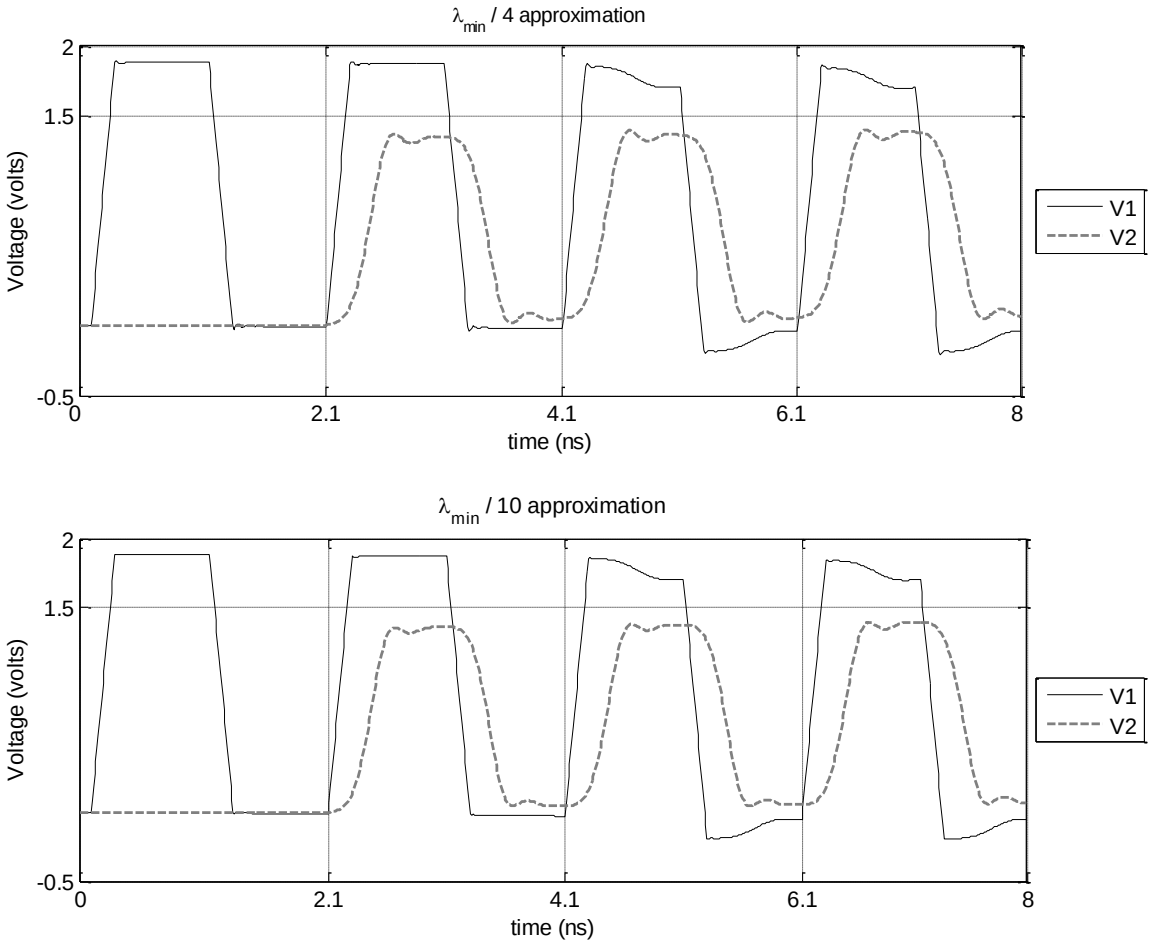

Figure 4.15: Transient analysis of the micro-strip line with $\lambda_{min}/4$ and $\lambda_{min}/10$ approximation

4.4 Validation of the Methodology

The methodology was verified by comparing it with the W-element feature which comes packaged with HSPICE. The circuit used for validation is shown in Figure 4.16. Each line in the two line system ($L = 20$ cm), driven and terminated independently, is electrically isolated from the other. This allows us to model them separately as two separate single-conductor transmission lines without having to consider cross-talk and interference between them. Each line has the following per unit length parameters: $\boldsymbol{\mathcal{L}} = 5$ nH/cm, $\boldsymbol{\mathcal{C}} = 0.5$ pF/cm, $\boldsymbol{\mathcal{R}} = 0.1\ \Omega$/cm, $\boldsymbol{\mathcal{G}} = 0.0001$ S/cm. The data used for the fit are obtained from the analytical expressions of the elements of the impedance and admittance matrices using transmission line theory [18]. The skin effect resistance matrix and the dielectric loss conductance matrix were ignored in both the approaches for the sake of simplicity. Hence, the per unit length inductance $\boldsymbol{\mathcal{L}}$ and per unit length conductance $\boldsymbol{\mathcal{G}}$ are not dependent on frequency. One line was modeled with the W-element capability of HSPICE. The other line was modeled using our approach with $\mathbf{Z_h}$ and $\mathbf{Y_h}$ represented as:

$$\mathbf{Z_h}(\omega) \triangleq h\, \mathbf{Z_{pul}}(\omega) \tag{4.11}$$

$$\mathbf{Y_h}(\omega) \triangleq h\, \mathbf{Y_{pul}}(\omega) \tag{4.12}$$

where $L = kh$, where k is an integer. The minimum allowable segment of the transmission line was bound by the quarter wavelength approximation. HSPICE was used to perform a simultaneous transient analysis on the two different line models and the waveforms were qualitatively compared. The results of the simulation experiment are given in Figure 4.17.

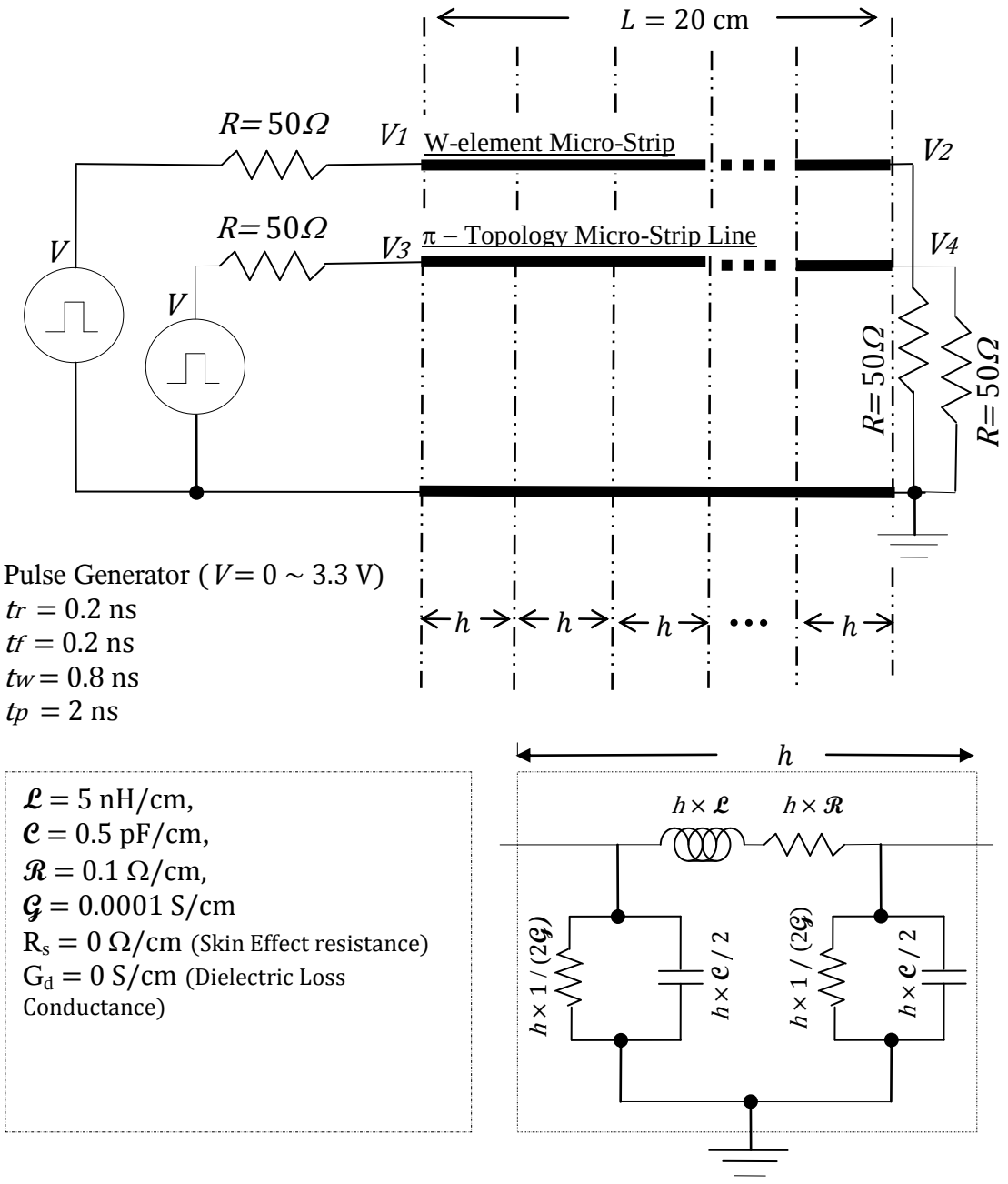

Figure 4.16: Circuit used for validation of methodology

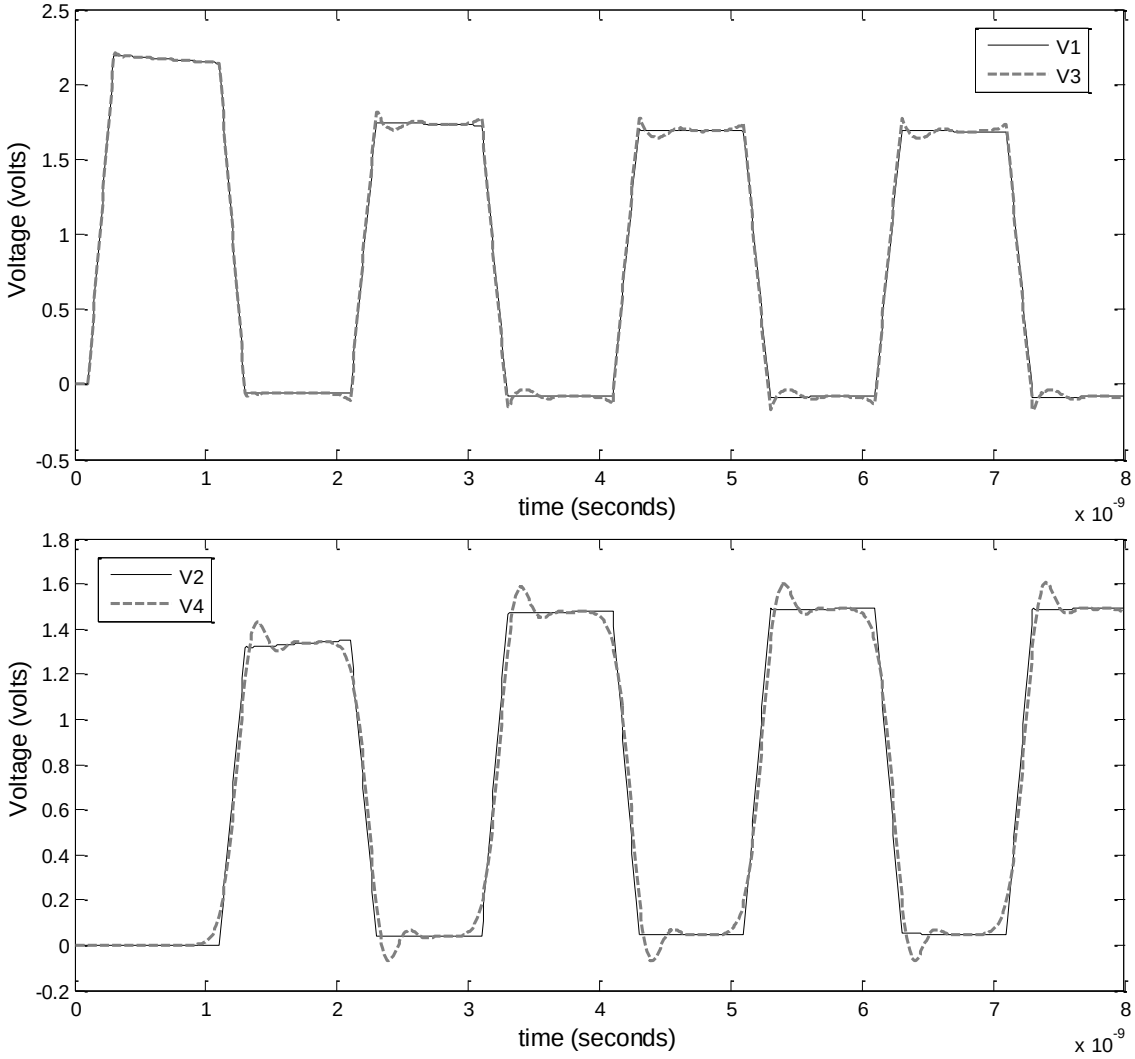

Figure 4.17: Plot of transient analysis of W-element vs π-network topology

The waveform with sharp corners is the W-element representation of the signal propagation, while the one with peaks is the representation through our approach. The two approaches seem to agree considerably with each other in terms of delay and attenuation. A qualitative comparison was also made between the Y-parameters generated analytically using MATLAB, the Y-parameters generated through W-element modeling and the Y-parameters generated using our approach. The results of the comparison are shown in Figures 4.18 and 4.19.

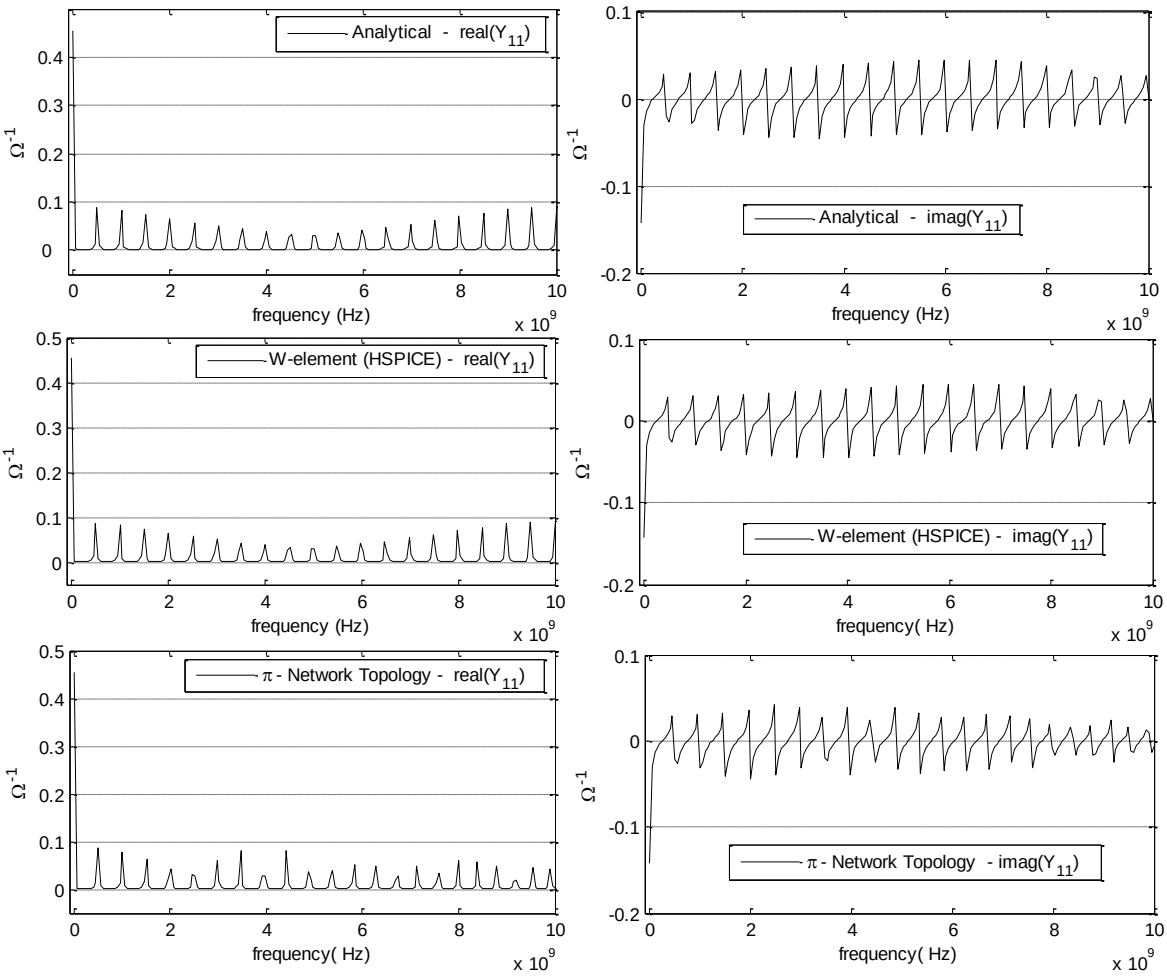

Figure 4.18: Comparison of Y_{11} obtained from analytical results, W-element simulation and our approach

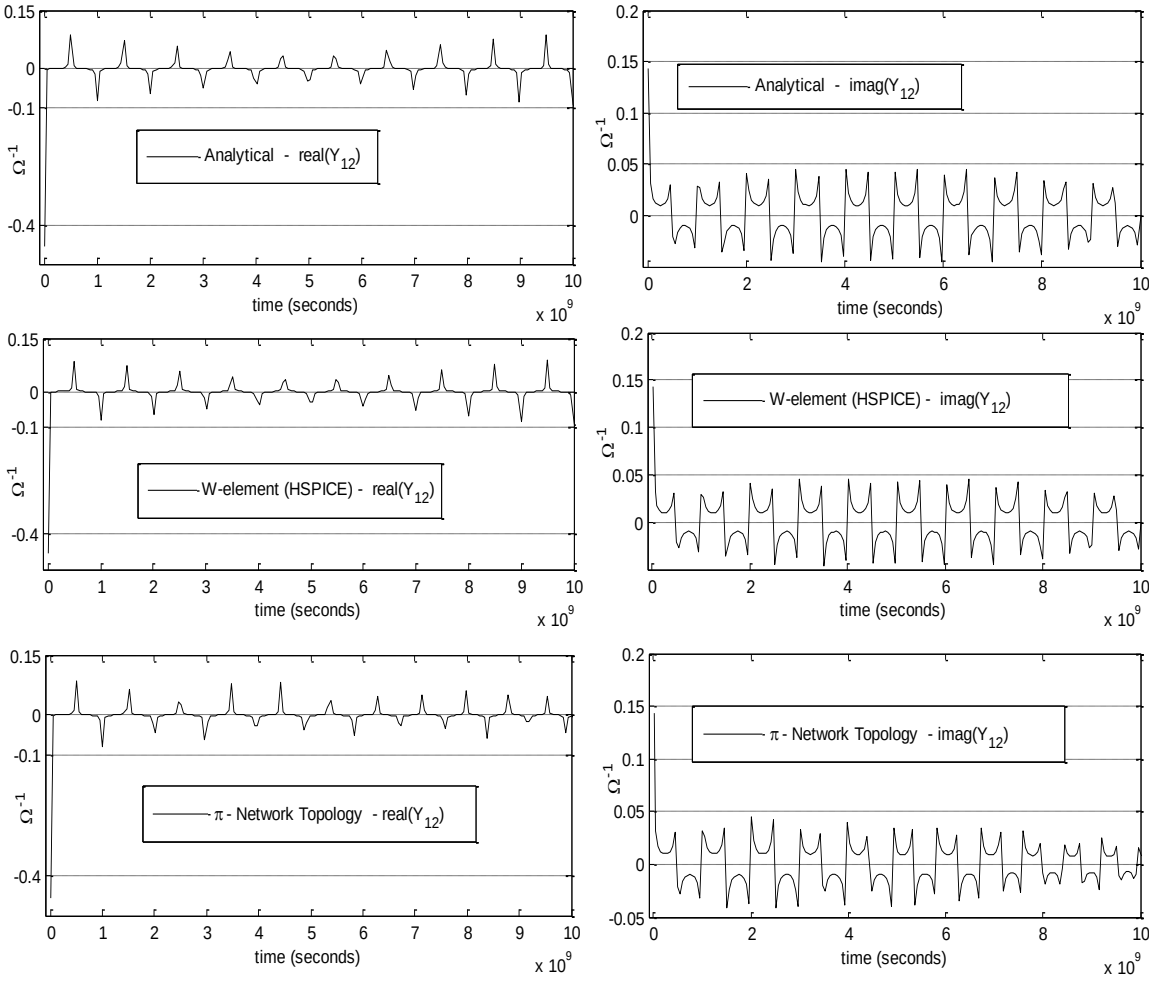

Figure 4.19: Comparison of Y_{12} obtained from analytical results, W-element simulation and our approach

4.5 Computational Efficiency: UIUC2D vs. π–Network Topology

The comparison of the computational efficiency of the UIUC2D approach with the π–network topology approach was based on the transient simulation results of a three-conductor example, the geometry of which is shown in Figure 4.20.

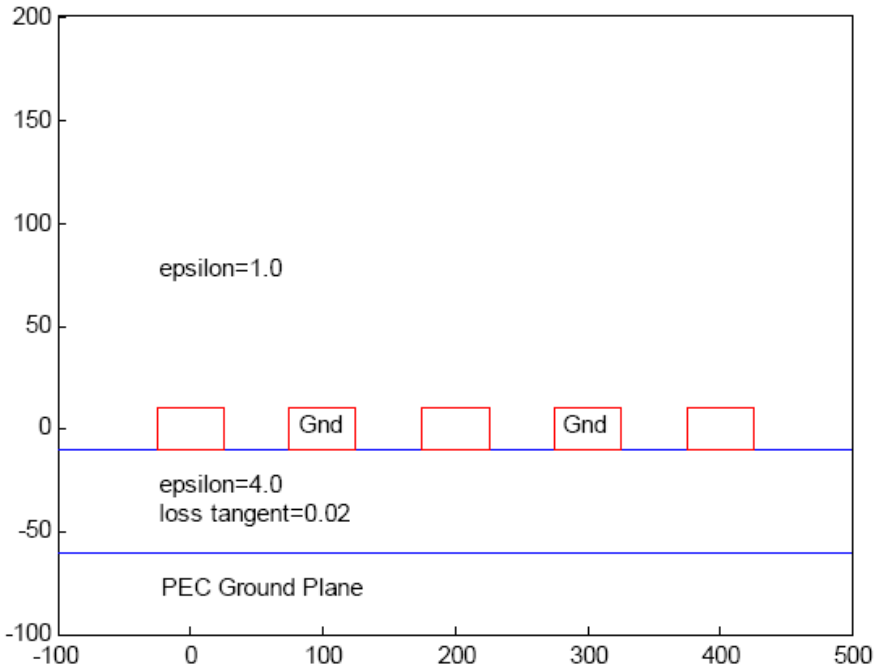

Figure 4.20: The three-conductor example

UIUC2D requires that the length of each segment for daisy-chaining into a transmission line should be no greater than l_{max}, which is defined by the following equation:

$$l_{max} = 0.1\frac{v_p}{f_{max}} \tag{4.13}$$

where $f_{max}=\frac{0.5}{t_r}$.

To ensure compatibility with the requirements of the UIUC2D approach, the value of lumped approximation was chosen to be $\lambda_{min}/10$ instead of $\lambda_{min}/4$. The length of the transmission line was arbitrarily chosen to be 5 cm. The number of frequency points to capture the p.u.l. transmission line parameters was chosen to be 20. A quadratic frequency sweep was again performed from 1 MHz to 10 GHz. The maximum allowable length of the transmission line segment for $\lambda_{min}/10$ lumped approximation was 0.18662 cm.

The HSPICE transient analysis for the three-interconnect structure as shown in Figure 4.21 took 0.50 s and 24.55 s for the transmission line models developed using the UIUC2D and the π–network topology approaches, respectively. The results of the simulation are shown in Figures 4.22 and 4.23, respectively.

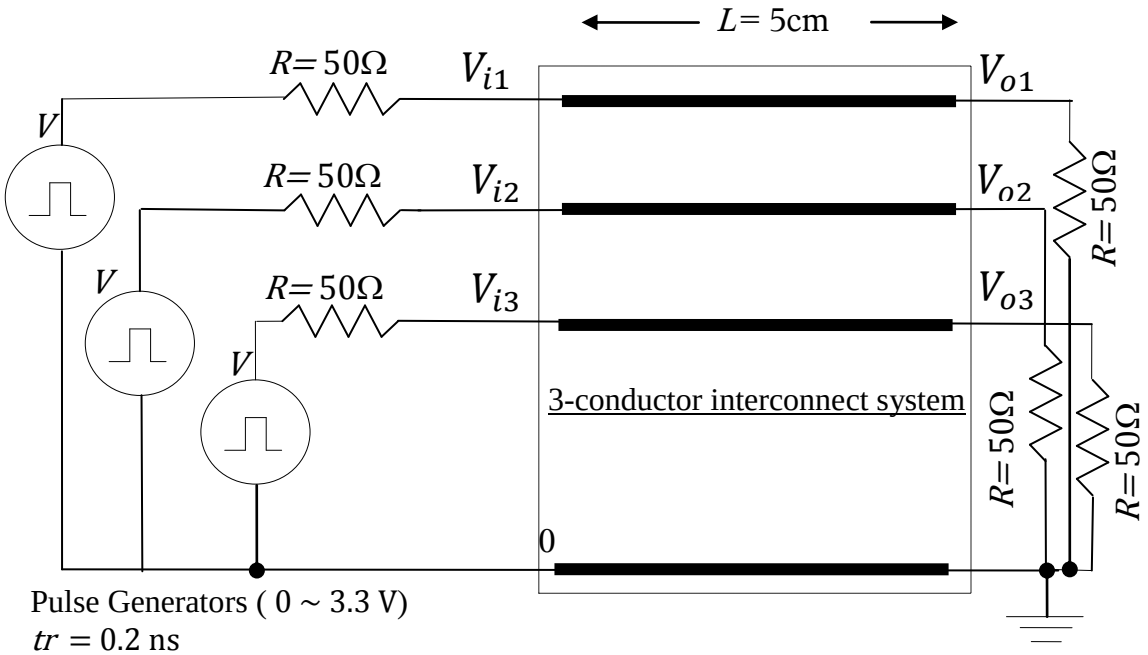

Pulse Generators (0 ~ 3.3 V)
tr = 0.2 ns
tf = 0.2 ns
tw = 0.8 ns
tp = 2 ns

$$h = \frac{L}{\left\lceil \frac{L}{h_{max}} \right\rceil} = 0.18519 \text{ cm } < h_{max} = 0.1\,\lambda_{min} = 0.1 \times 1.8662$$

$$= 0.18662 \text{ cm}$$

$$L = h \left\lceil \frac{L}{h_{max}} \right\rceil = 0.18519 \times 27 = 5 \text{ cm}$$

Figure 4.21: Circuit used for transient simulation of three-conductor system

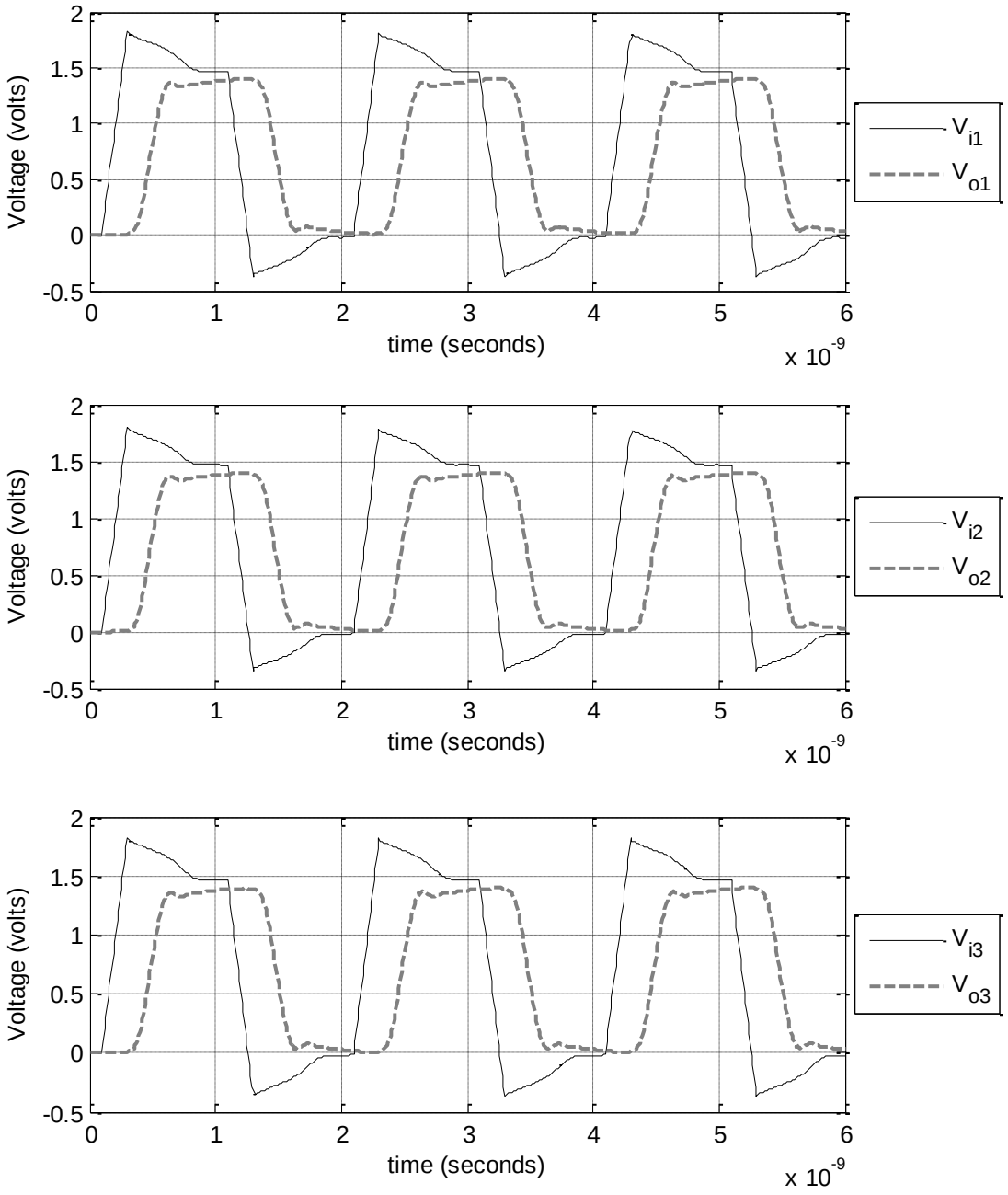

Figure 4.22: Transient simulation results using the UIUC2D approach

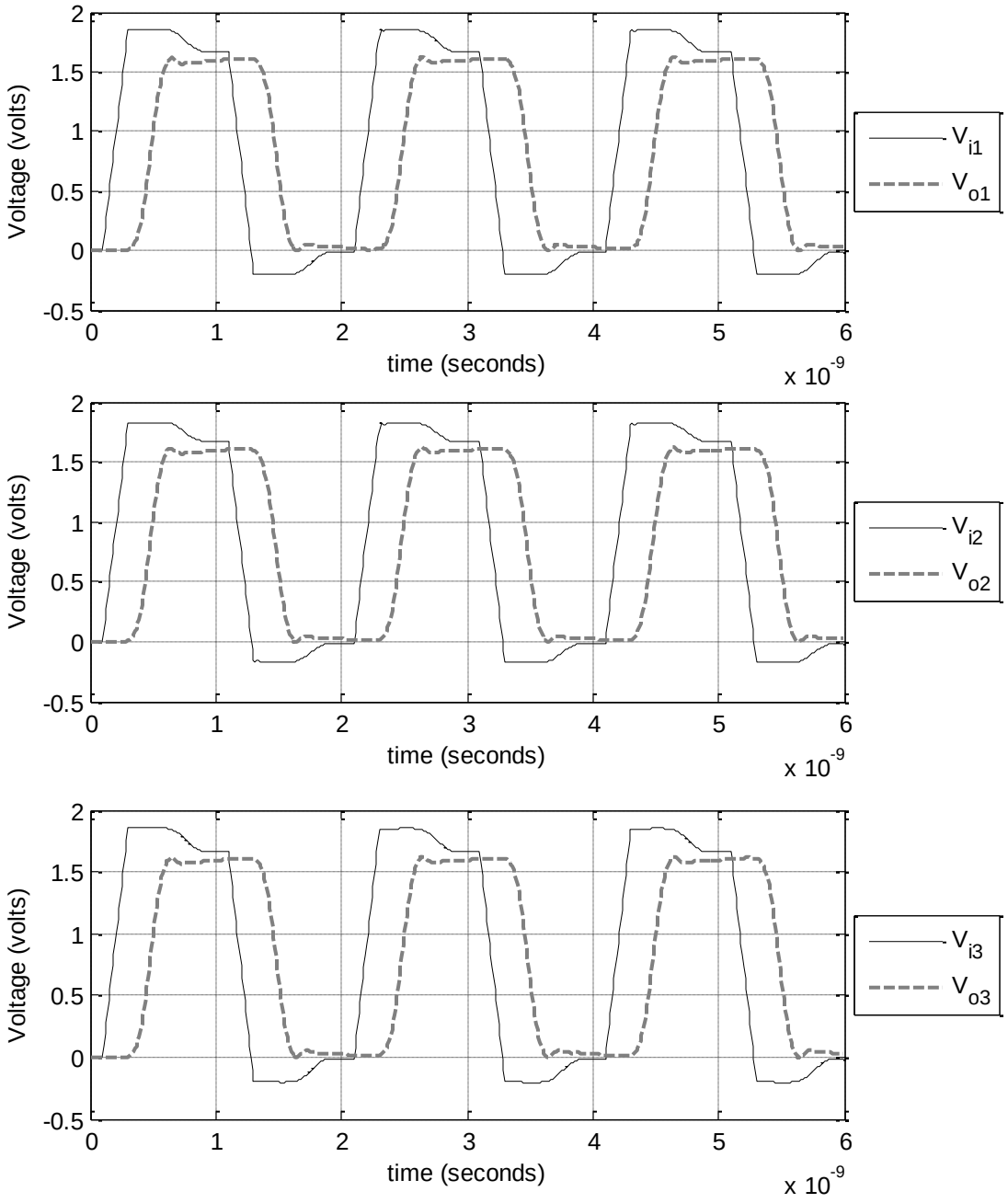

Figure 4.23: Transient simulation results using the π–network topology approach

4.6 Correlation Between Number of Segments and the Attenuation Factor

To investigate the dependence of transient analysis on the number of sections into which the transmission line is segmented, the micro-strip line shown in Figure 4.24 was used. The length of the line was chosen to be 20 cm and the value of lumped approximation was chosen to be $\lambda_{min}/4$. A quadratic sweep was performed from 1 MHz to 20 GHz for a total of 20 different frequency points giving the value of 0.45639 cm for h_{max}, the maximum allowable length for lumped approximation, to hold. The number of poles needed for fitting was four. Two separate cases were simulated, one with size of each segment equal to 0.45455 cm and the other with 0.22727 cm, corresponding to 44 and 88 sections, respectively. The results of the transient analysis performed on both cases are shown in Figure 4.25.

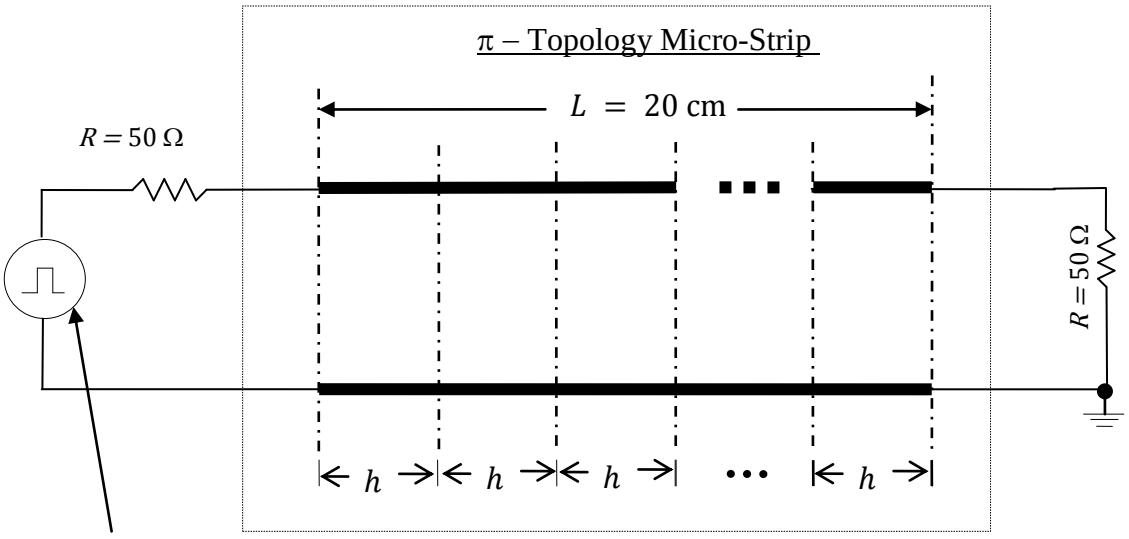

Pulse Generator (0 ~ 3.3 V)
tr = 0.2ns
tf = 0.2 ns
tw = 0.8 ns
tp = 2 ns

$$h = \frac{L}{\left\lceil \frac{L}{h_{max}} \right\rceil} < h_{max} = 0.25\,\lambda_{min} = 0.45639 \text{ cm}$$

Case 1: $L = h \left\lceil \frac{L}{h_{max}} \right\rceil = 0.45455 \times 44 = 5$ cm

Case 2: $L = h \left\lceil \frac{L}{h_{max}} \right\rceil = 0.22727 \times 88 = 5$ cm

Figure 4.24: Circuit used for transient analysis

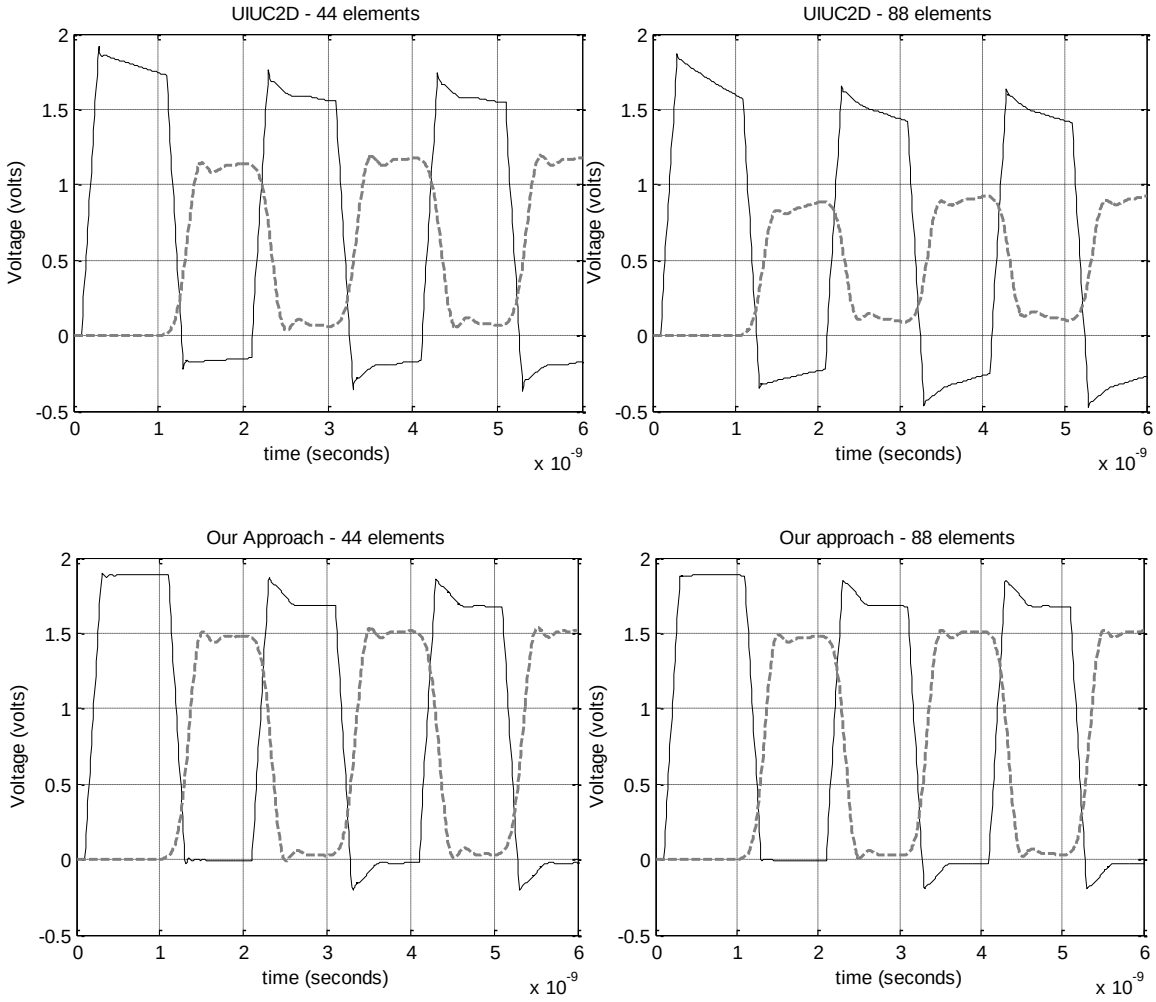

Figure 4.25: Transient analysis plots for 44 and 88 segments using UIUC2D and our approach

It is observed in Figure 4.25 that, for the π–network topology approach, the results of the transient simulation were impervious to the choice of the number of segments if the lumped approximation criterion was satisfied. However, for the UIUC2D approach it was observed that the choice of the number of segments affected the results of the transient simulation even when the lumped approximation criterion was satisfied.

4.7 Reciprocity and Symmetry Analysis

One of the fundamental principles governing passive networks is the reciprocity theorem, which states that for a passive linear system, the response is the same when the source and the measurer are interchanged. In terms of network parameters, like the Y-parameters, this entails that $Y_{ij} = Y_{ji}$. In order to compare the reciprocity of the models generated using the UIUC2D approach with that of the π–network topology approach, network analysis was performed on a micro-strip line of length 20 cm as shown in Figure 4.26. The cross-sectional geometry and the parameters of model generation were chosen the same way as described in Section 4.2. The resulting Y-parameter plots are shown in Figures 4.27 and 4.28.

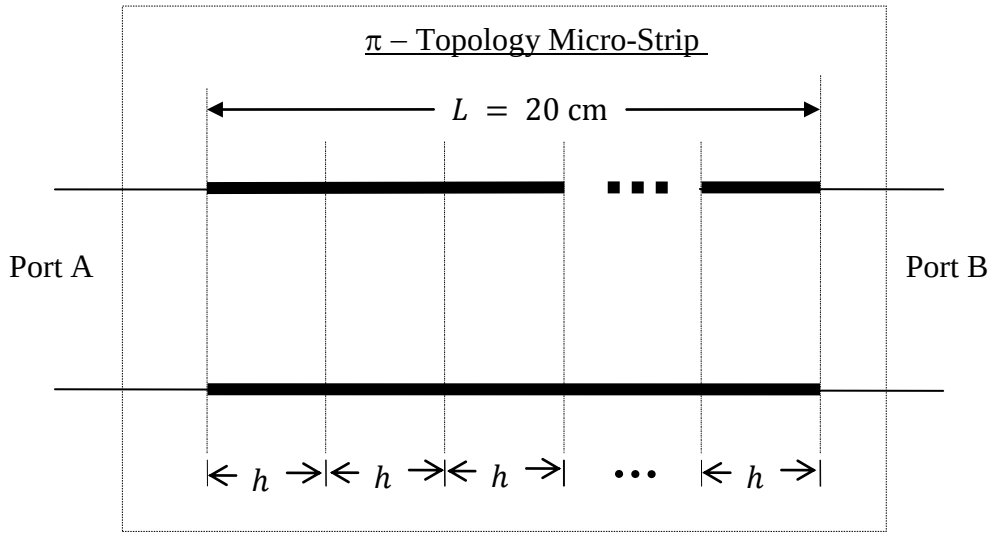

$$h = \frac{L}{\left\lceil \frac{L}{h_{max}} \right\rceil} = 0.45455 \text{ cm} < h_{max} = 0.25\,\lambda_{min} = 0.45639 \text{ cm}$$

$$L = h\left\lceil \frac{L}{h_{max}} \right\rceil = 0.45455 \times 44 = 20 \text{ cm}$$

Figure 4.26: Circuit used for two-port network analysis

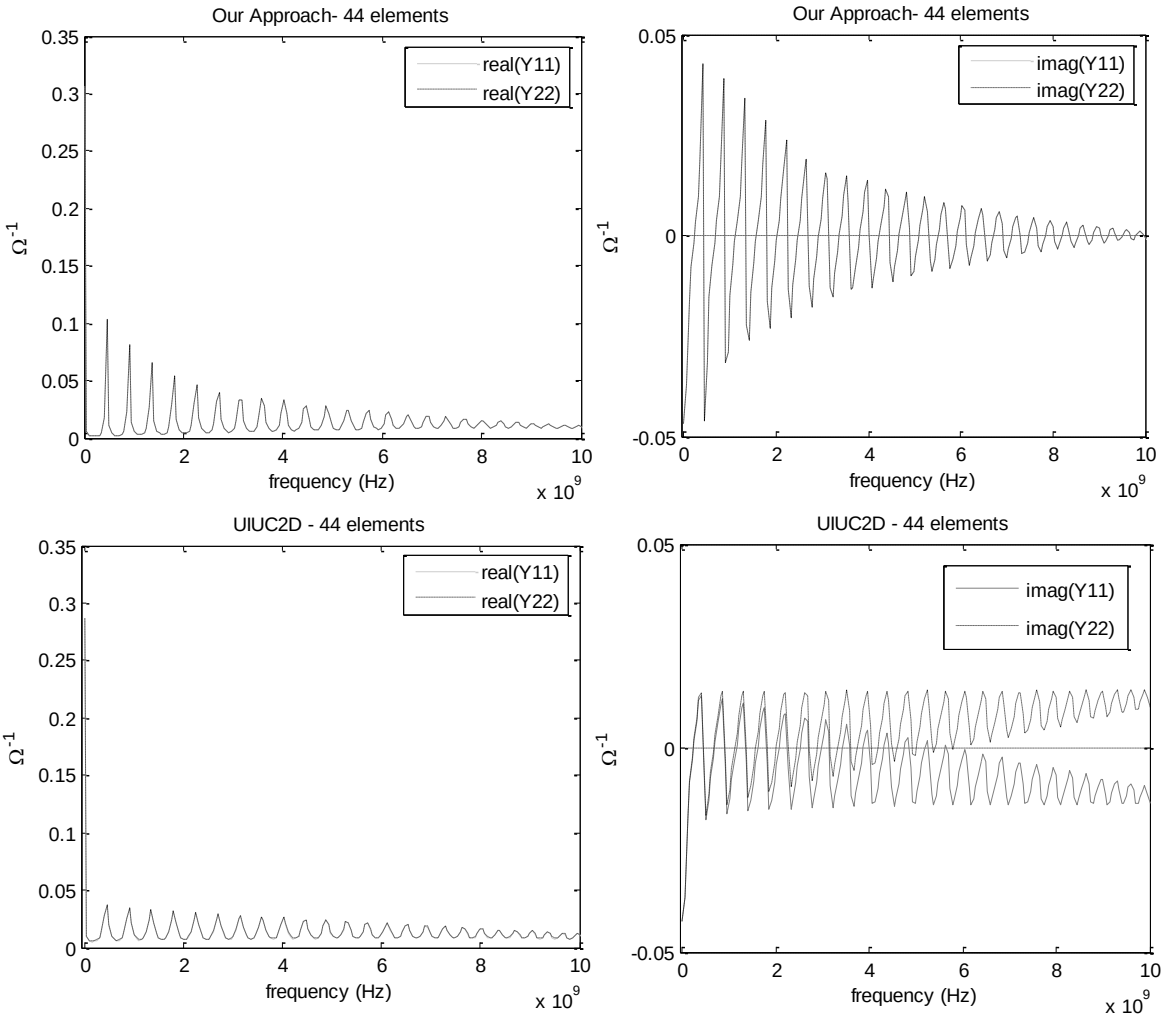

Figure 4.27: Comparing the Y_{11} and Y_{22} parameters of our approach with the UIUC2D model

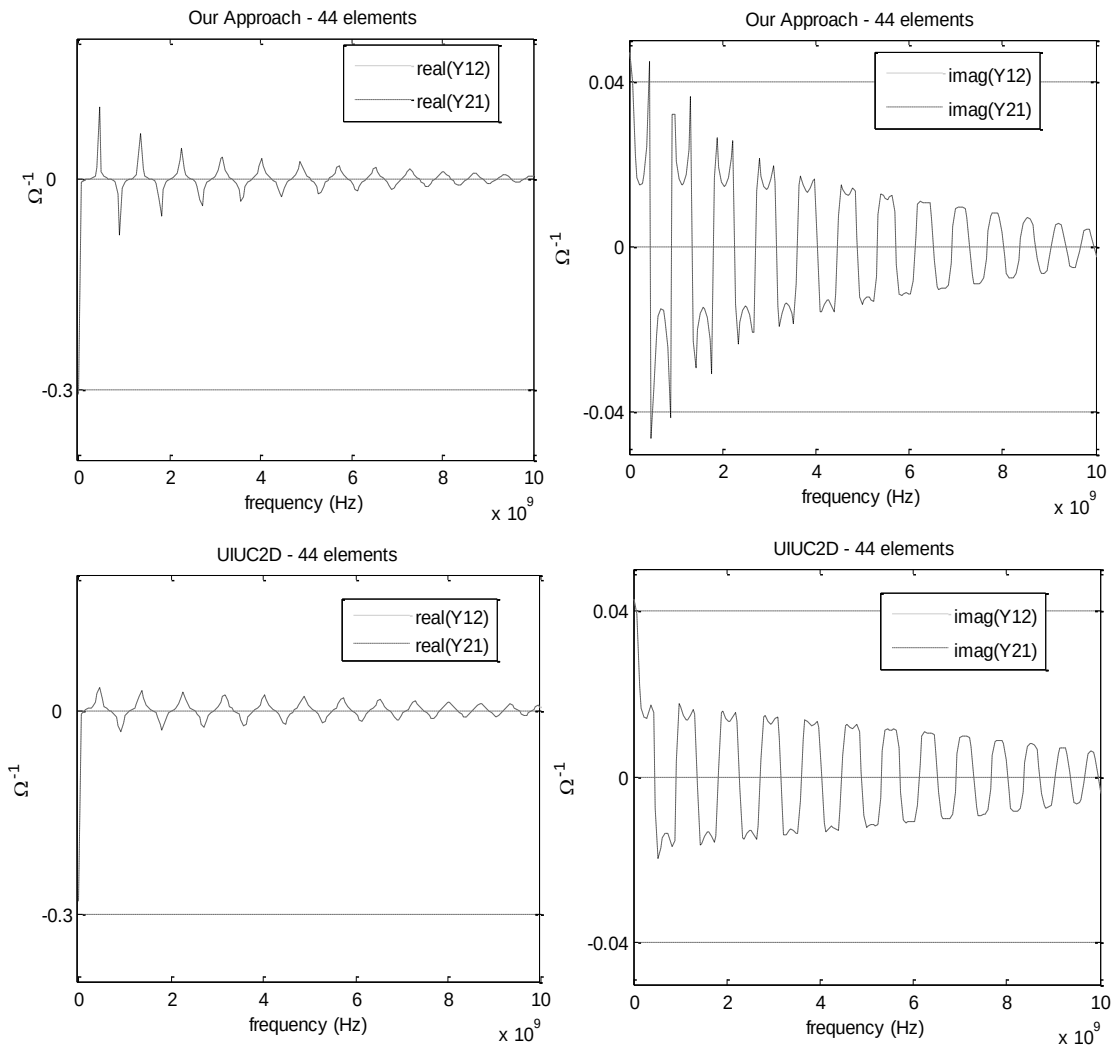

Figure 4.28: Comparing the Y_{21} and Y_{12} parameters of our approach with the UIUC2D model

CHAPTER 5

CONCLUSIONS

5.1 Summary

An alternative equivalent circuit generation scheme was presented with examples to demonstrate the implementation. The examples show that the model is applicable to all ranges of physical dimensions, lengths, frequencies, and arbitrary terminations of interest. The developed models can accurately predict the electromagnetic behavior of multi-conductor transmission lines for interconnect bandwidths approaching 10 GHz. The alternate scheme, although computationally more expensive, is reciprocal and the transient results are not affected by number of segments. The generated macro-models also satisfy certain properties of physical systems including real time domain response, causality, stability, and passivity.

5.2 Future Work

The methodology presented in this work can be readily extended to interconnects of higher dimensions (more than three). The spatial and temporal complexity of the HPSICE simulations can be reduced considerably by employing model order reduction (MOR) algorithms. MOR techniques require knowledge of the state-space expression of the original system in order to generate the reduced order system. The algorithms employed for rational function approximation also generate state-space models of the input-output characteristics of the passive physical systems. These reduced order macro-models could be used to generate less computationally intensive netlists for HPSICE simulations.

REFERENCES

[1] E. Bogatin, *Signal Integrity – Simplified.* Upper Saddle River, NJ: Pearson Education, Inc., 2004

[2] L. Green, "Understanding the importance of signal integrity," *Circuits and Devices Magazine, IEEE,* vol. 15, no. 6, pp. 7 – 10, Nov. 1999.

[3] G. V. Kopcsay, B. Krauter, D. Widiger, A. Deutsch, B. J. Rubin, and H. H. Smith, "A comprehensive 2-D inductance modeling approach for VLSI interconnects: Frequency-dependent extraction and compact circuit model synthesis," *IEEE Transactions on Very Large Scale Integration (VLSI) Systems,* vol. 10, no. 6, pp. 695-711, Dec. 2002.

[4] A. Deutsch *et al., "*On-chip wiring design challenges for gigahertz operation," in *Proceedings of the IEEE,* vol. 89, no. 4, pp. 529-548, Apr. 2001.

[5] A. Deutsch *et al., "*Frequency-dependent crosstalk simulation for on-chip interconnections," *IEEE Transactions on Advanced Packaging,* vol. 22, no. 3, pp. 292-308, Aug. 1999.

[6] C. R. Paul, *Analysis of Multiconductor Transmission Lines.* New York, NY: Wiley, 1994.

[7] A. Woo, "SPICE implementation of an optimal discrete model for dispersive transmission-line modeling of interconnections," M.S. thesis, University of Illinois at Urbana-Champaign, IL, USA, 2003.

[8] J. Morsey, K. Coperich, V. Okhmatovski, A. C. Cangellaris, and A. Ruehli, "A new broadband transmission line model for accurate simulation of dispersive interconnects," in *Proceedings of 3rd Electronics Packaging Technology Conference,* pp. 345-351, Dec. 2000.

[9] K. Coperich, J. Morsey, V. Okhmatovski, A. C. Cangellaris, and A. E. Ruehli, "Systematic development of transmission line models for interconnects with frequency-dependent losses," *IEEE Transactions on Microwave Theory and Techniques,* vol. 49, pp. 1677-1685, Oct. 2001.

[10] T. L. Quarles, "The SPICE3 implementation guide," Univ. California, Berkeley, Tech. Rep. ERL-M89/44, 1989.

[11] B. Young, *Digital Signal Integrity.* Upper Saddle River, NJ: Prentice-Hall, Inc., 2001.

[12] B. Gustavsen and A. Semlyen, "Rational approximation of frequency domain

responses by vector fitting," *IEEE Transactions of Power Delivery*, vol. 14, pp. 1052-1061, July 1999.

[13] B. Gustavsen, "Computer code for rational approximation of frequency dependent admittances," *IEEE Transactions on Power Delivery*, vol. 17, pp. 1093-1098, Oct. 2002.

[14] B. Gustavsen and A. Semlyen, "Enforcing passivity for admittance matrices approximated by rational functions," *IEEE Transactions of Power Systems*, vol. 16, pp. 97-104, Feb. 2001.

[15] P. Silvester, "Model network theory of skin effect in flat conductors," *Proceedings of the IEEE*, vol. 54, pp. 1147-1151, Sept. 1996.

[16] K. Coperich, "Rigorous electromagnetic modeling of conductor and substrate losses for high-speed interconnect structures," Ph.D. dissertation, University of Illinois at Urbana-Champaign, IL, USA, 2001.

[17] *UIUC2D Manual (Version 2.0)*, Center for Computational Electromagnetics and Electromagnetics Lab, Department of Electrical and Computer Engineering, University of Illinois at Urbana-Champaign, IL, USA.

[18] S. Ramo, J. R. Whinnery, and T. V. Duzer, *Fields and Waves in Communication Electronics*. New York, NY: John Wiley & Sons, Inc., 1994.